

---

# Provable Robust Saliency-based Explanations

---

Chao Chen<sup>1</sup> Chenghua Guo<sup>2</sup> Guixiang Ma<sup>3</sup> Ming Zeng<sup>4</sup> Xi Zhang<sup>2</sup> Sihong Xie<sup>1</sup>

## Abstract

Robust explanations of machine learning models are critical to establish human trust in the models. The top- $k$  intersection is widely used to evaluate the robustness of explanations. However, most existing attacking and defense strategies are based on  $\ell_p$  norms, thus creating a mismatch between the evaluation and optimization objectives. To this end, we define explanation thickness for measuring top- $k$  salient features ranking stability, and design the *R2ET* algorithm based on a novel tractable surrogate to maximize the thickness and stabilize the top salient features efficiently. Theoretically, we prove a connection between R2ET and adversarial training; using a novel multi-objective optimization formulation and a generalization error bound, we further prove that the surrogate objective can improve both the numerical and statistical stability of the explanations. Experiments with a wide spectrum of network architectures and data modalities demonstrate that R2ET attains higher explanation robustness under stealthy attacks while retaining model accuracy.

## 1. Introduction

Deep neural networks (DNNs) have proven their strengths in many real-world applications (Wang et al., 2020b; Zhou et al., 2020; Hudson & Cohen, 2000). The explainability of DNNs is a fundamental requirement for establishing humans’ trust and is key to further deployments in high-stake applications (Goodman & Flaxman, 2017; Pu & Chen, 2006). The explanations also help improve the prediction performance (Rieger et al., 2020) and robustness (Boopathy et al., 2020). Among all explanation methods, saliency maps based on model gradients with respect to inputs are widely adopted due to their inexpensive computation and intuitive interpretation (Nielsen et al., 2022). However, existing works (Dombrowski et al., 2019; Ghorbani et al., 2019; Heo et al., 2019) show that the gradients can be manipulated with unnoticeable changes in the input. Since human cognitive capability is limited (Saaty & Ozdemir, 2003), an explanation typically attributes a prediction to a few salient

features of the input data, and the top- $k$  intersection (Wang & Kong, 2022; Wang et al., 2020c; Chen et al., 2019b) is widely used to evaluate the robustness of explanations (see Fig. 1).

**Challenges.** Existing works (Dombrowski et al., 2021; Wang et al., 2020c; Chen et al., 2019b; Dombrowski et al., 2019) study the explanation robustness through  $\ell_p$  distance, leading to the idea of smoothing the curvature for robust explanations. However, as demonstrated in Fig. 1, a perturbed explanation with a small  $\ell_p$  distance to the original one can have rather different top salient features, since the  $\ell_p$  norm considers the importance of *all* features equally. Such inconsistency between the  $\ell_p$  metric and the modus operandi of human perception (represented by top- $k$  intersection) can lead to imprecise measures of explanation robustness. Thus, we propose explanation thickness to precisely quantify the stability of the rankings of the top salient features. Besides that, adversarial training (AT) (Wang et al., 2012; Ivankay et al., 2020; Singh et al., 2020; Wang & Kong, 2022; Sarkar et al., 2021) has been used for robust explanations using adversarial samples. However, AT is time-consuming since it needs to update the adversarial sample for each training iteration. Thus, we propose to expedite the training for robust explanations by effective and efficient regularizers and bypass AT.

**Contributions.** We center our contributions around a novel metric called “ranking explanation thickness” that precisely measures the robustness of the top salient features. (1) Theoretically, we derive a surrogate loss based on bounds of ranking explanation thickness for more efficient optimization and to reveal a fundamental limit of using Hessian norm for explanation robustness. We also disclose the equivalence between the proposed objective and Adversarial Training in Eq. (7). Sec. 4 justifies maximizing thickness for explanation robustness. (2) Algorithmically, based on the theoretical analysis, we propose an efficient training method, R2ET, to attain the desired robustness without costly AT. R2ET optimizes the surrogate bounds to overcome the limitation of existing Hessian-based curvature smoothing approaches. (3) Experimentally, we conduct both  $\ell_2$  norm attack and a ranking-based attack (see Fig. 1) to demonstrate that: *i*) prior  $\ell_p$  norm attack cannot manipulate explanations as effectively as ranking-based attacks, and R2ET outperforms state-of-the-art methods, including Hessian-related defense

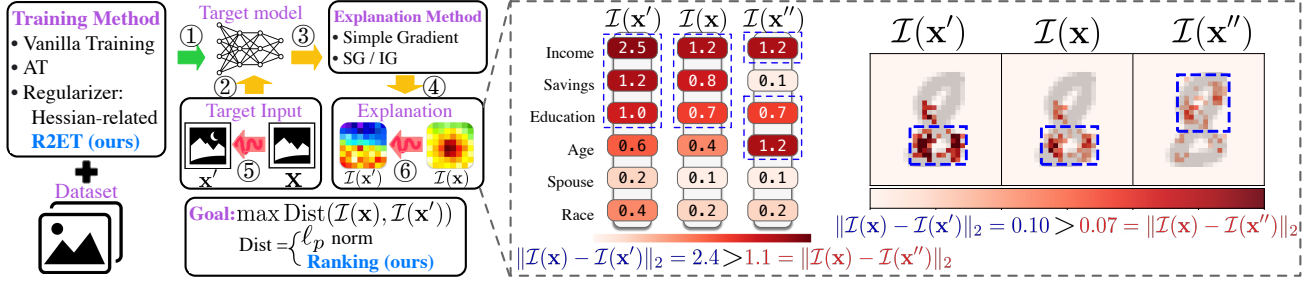


Figure 1: **Left:** Green (①): Model training. Yellow (②-④): Explanation generation for a target input. Red (⑤-⑥): Adversarial attacks against the explanation by manipulating the input. **Right:** Two examples of the saliency maps (explanations) show that smaller  $\ell_p$  distances do not imply similar top salient features.  $\mathcal{I}(\mathbf{x}'')$  has a smaller  $\ell_2$  distance from the original explanation  $\mathcal{I}(\mathbf{x})$ , but manipulates the explanation more significantly (by top- $k$  metric) shown in blue dashed boxes. Statistically,  $\mathcal{I}(\mathbf{x}')$  has a 67% top-3 overlap in the tabular case, and 36% top-50 overlap in the image, compared with  $\mathcal{I}(\mathbf{x}')$ 's 100% and 92% top- $k$  overlap, respectively.

algorithms and AT, concerning robust rankings; *ii*) the high correlation between explanation thickness and robustness; *iii*) the generality and wide applications of R2ET to different neural network architectures and various data modalities.

## 2. Preliminaries

**Saliency map explanations.** Let a classification model with parameters  $\mathbf{w}$  be  $f(\mathbf{x}, \mathbf{w}) : \mathcal{X} \rightarrow [0, 1]^C$ , and  $f_c(\mathbf{x}, \mathbf{w})$  is the probability of class  $c$  for the input  $\mathbf{x} \in \mathcal{X}$ . A saliency map explanation (Adebayo et al., 2018; Baldassarre & Azizpour, 2019) is defined as  $\mathcal{I}(\mathbf{x}, c; f) = \nabla_{\mathbf{x}} f_c(\mathbf{x}, \mathbf{w})$ . Since  $f$  is fixed for explanations, we omit  $\mathbf{w}$  and fix  $c$  to the predicted class. We denote  $\mathcal{I}(\mathbf{x}, c; f)$  by  $\mathcal{I}(\mathbf{x})$ , and the  $i$ -th feature's importance score by  $\mathcal{I}_i(\mathbf{x})$ .

**Threat model.** The adversary solves the following problem to find the optimal perturbation  $\delta^*$  to distort the explanations without changing the predictions (Dombrowski et al., 2021):

$$\begin{aligned} \max_{\delta} \quad & \text{Dist}(\mathcal{I}(\mathbf{x}), \mathcal{I}(\mathbf{x} + \delta)) \\ \text{s.t.} \quad & \arg \max_c f(\mathbf{x})_c = \arg \max_c f(\mathbf{x} + \delta)_c, \quad \|\delta\|_2 \leq \epsilon. \end{aligned} \quad (1)$$

$\delta$  is the perturbation whose  $\ell_2$  norm is not larger than a given budget  $\epsilon$ .  $\text{Dist}(\cdot, \cdot)$  evaluates how different the two explanations are. E.g.,  $\text{Dist}(\cdot, \cdot)$  is inversely related to the correlation between two rankings of features. The constraint can make the manipulations more difficult (see Sec. 4). We tackle constraints with constrained optimization (see B.6.4) and will not explicitly show the constraints.

## 3. Explanation Robustness via Thickness

### 3.1. Ranking explanation thickness

**Quantify the gap.** Given a model  $f$  and the associated original explanation  $\mathcal{I}(\mathbf{x})$  with respect to an input  $\mathbf{x} \in \mathbb{R}^n$ , we denote the *gap* between the  $i$ -th and  $j$ -th features' importance by  $h(\mathbf{x}, i, j) = \mathcal{I}_i(\mathbf{x}) - \mathcal{I}_j(\mathbf{x})$ . Clearly,  $h(\mathbf{x}, i, j) > 0$

*if and only if* the  $i$ -th feature has a more positive contribution to the prediction than the  $j$ -th feature. Although the feature importance order varies across different  $\mathbf{x}$ , for notation simplicity, we label the features in descending order such that  $h(\mathbf{x}, i, j) > 0, \forall i < j$ , holds for any *original* input  $\mathbf{x}$ . This assumption will not affect the following analysis.

**Ranking robustness.** Ranking robustness (Goren et al., 2018; Zhou & Croft, 2006) measures how much the ranking changes concerning slight input perturbations. Apparently, the adversary in Eq. (1) searches the perturbed input  $\mathbf{x}' = \mathbf{x} + \delta$  with  $\|\delta\|_2 \leq \epsilon$  to flip the ranking between  $(i, j)$  features such that  $h(\mathbf{x}', i, j) < 0$  for some  $i < j$ . Meanwhile, the defender tries to retain the rankings,  $h(\mathbf{x}', i, j) > 0, \forall i < j$ . We define the *explanation thickness* by the probability of the relative ranking of the features  $(i, j)$  being unchanged in a neighborhood of  $\mathbf{x}$ . The relevant work (Yang et al., 2020a) proposes the boundary thickness to evaluate a model's *prediction* robustness by measuring the expected distance between two level sets.

**Definition 3.1** (Local pairwise ranking thickness). Given a model  $f$ , an input  $\mathbf{x} \in \mathcal{X}$  and a distribution  $\mathcal{D}$  of  $\mathbf{x}' \in \mathcal{X}$ , the local pairwise ranking thickness (as a probability) of the pair of features  $(i, j)$  is

$$\tilde{\Theta}(f, \mathbf{x}, \mathcal{D}, i, j) \stackrel{\text{def}}{=} \mathbb{E}_{\mathbf{x}' \sim \mathcal{D}} \left[ \int_0^1 \mathbb{1}[h(\mathbf{x}(t), i, j) \geq 0] dt \right], \quad (2)$$

where  $\mathbf{x}' \sim \mathcal{D}$  is the perturbed input drawn from a neighborhood of  $\mathbf{x}$  according to  $\mathcal{D}$ .  $\mathbf{x}(t) = (1-t)\mathbf{x} + t\mathbf{x}'$ ,  $t \in [0, 1]$ , is on the line segment connecting the sample pair  $(\mathbf{x}, \mathbf{x}')$ .

Clearly,  $\tilde{\Theta} \leq 1$  and the equality holds when the relative importance of the  $i$ -th and  $j$ -th features is never flipped. The integration calculates the probability that the  $i$ -th feature is more important than  $j$ -th feature between  $\mathbf{x}$  and  $\mathbf{x}'$ . The expectation makes the thickness estimation more comprehensive by considering all potential perturbed inputs  $\mathbf{x}' \sim \mathcal{D}$ , where  $\mathcal{D}$  can be an Uniform distribution  $U(\mathbf{x}, \epsilon)$  (Wang et al., 2020c) or a Gaussian distribution  $\mathcal{N}(\mathbf{x}, \sigma^2 I)$  (Smilkov et al., 2017). Alternatively,  $\mathbf{x}'$  can be an adver-

serial sample local to  $\mathbf{x}$  (Yang et al., 2020a), and we will further discuss it in Sec. 3.2.

**Relaxation.** The non-differentiability of the indicator function in Eq. (2) prevents us from analyzing and optimizing the thickness efficiently. Inspired by (Agarwal, 2011), we define the local pairwise ranking thickness by measuring the *expected gap* between the importance score of  $i$  and  $j$  features,

$$\Theta(f, \mathbf{x}, \mathcal{D}, i, j) \stackrel{\text{def}}{=} \mathbb{E}_{\mathbf{x}' \sim \mathcal{D}} \left[ \int_0^1 h(\mathbf{x}(t), i, j) dt \right], \quad (3)$$

which is still monotonically increasing in  $h$ .

**Top- $k$  thickness.** Existing works in general robust ranking propose maintaining the ranking between *every* two features (Zhou et al., 2021), demanding a complexity of  $\mathcal{O}(n^2)$  for  $n$  features. However, as shown in Fig. 1, only the top- $k$  important features in  $\mathcal{I}(\mathbf{x})$  and the robustness of their positions are more relevant to human perception of explanation. Thus, only the relative ranking between a top- $k$  salient feature and any other non-salient one is relevant. We define the following robustness metric that requires nearly-linear complexity  $\mathcal{O}(n)$  when  $k \ll n$ .

**Definition 3.2** (Local top- $k$  ranking thickness). Given a model  $f$ , an input  $\mathbf{x} \in \mathcal{X}$ , and a distribution  $\mathcal{D}$  of  $\mathbf{x}' \in \mathcal{D}$ , the local thickness of the ranking of the top- $k$  features is

$$\Theta(f, \mathbf{x}, \mathcal{D}; k, n) \stackrel{\text{def}}{=} \frac{1}{m} \sum_{i=1}^k \sum_{j=k+1}^n \Theta(f, \mathbf{x}, \mathcal{D}, i, j), \quad (4)$$

where  $m = k(n - k)$ .

### 3.2. Training for robust ranking explanations

Sec. 4 shows that maximizing the ranking explanation thickness can make attacks *numerically and statistically* more difficult and thus the explanation more robust. We propose to add  $\Theta(f, \mathbf{x}, \mathcal{D}; k, n)$  as a regularizer when training  $f(\mathbf{x}, \mathbf{w})$  on a training set  $(\mathcal{X}_T, \mathcal{Y}_T)$ :

$$\min_{\mathbf{w}} \mathcal{L}_{total}(f) = \mathcal{L}_{cls}(f) - \lambda \mathbb{E}_{\mathbf{x} \in \mathcal{X}_T} [\Theta(f, \mathbf{x}, \mathcal{D}; k, n)],$$

where  $\mathcal{L}_{cls}(f)$  is the empirical classification loss of  $f(\mathbf{x}, \mathbf{w})$  and  $\lambda > 0$  is a hyperparameter.

**A surrogate bound of explanation thickness.** Directly optimizing  $\Theta$  in Eq. (4) requires  $M_1 \times M_2 \times 2$  backward propagations *per* training sample *per* iteration.  $M_1$  is the number of  $\mathbf{x}'$  sampled from  $\mathcal{D}$ , or the number of iterations for finding the adversarial sample  $\mathbf{x}'$ ;  $M_2$  is the number of interpolations  $\mathbf{x}(t)$  sampled from the line segment between  $\mathbf{x}$  and  $\mathbf{x}'$ ; and evaluating the gradient of  $h(\mathbf{x}, i, j) = \mathcal{I}_i(\mathbf{x}) - \mathcal{I}_j(\mathbf{x})$  requires at least 2 backward propagations (Pearlmutter, 1994). To avoid sampling  $\mathbf{x}'$  and  $\mathbf{x}(t)$ , we derive a lower bound of  $\Theta$ , which requires only 2 backward propagations each time.

**Definition 3.3** (Locally Lipschitz continuity). A function  $f$  is  $L$ -locally Lipschitz continuous if  $\|f(\mathbf{x}) - f(\mathbf{x}')\|_2 \leq L\|\mathbf{x} - \mathbf{x}'\|_2$  holds for all  $\mathbf{x}' \in \mathcal{B}_2(\mathbf{x}, \epsilon) = \{\mathbf{x}' \in \mathbb{R}^n : \|\mathbf{x} - \mathbf{x}'\|_2 \leq \epsilon\}$ .

**Proposition 3.4.** (Bounds of thickness) *Given a  $L$ -locally Lipschitz model  $f$ , for some  $L > 0$ , local pairwise ranking thickness  $\Theta(f, \mathbf{x}, \mathcal{D}, i, j)$  is bounded by*

$$\begin{aligned} h(\mathbf{x}, i, j) - \epsilon * \frac{1}{2} \|H_i(\mathbf{x}) - H_j(\mathbf{x})\|_2 &\leq \\ \Theta(f, \mathbf{x}, \mathcal{D}, i, j) &\leq h(\mathbf{x}, i, j) + \epsilon(L_i + L_j), \end{aligned} \quad (5)$$

where  $H_i(\mathbf{x})$  is the derivative of  $\mathcal{I}_i(\mathbf{x})$  with respect to  $\mathbf{x}$ , and  $L_i = \max_{\mathbf{x}' \in \mathcal{B}_2(\mathbf{x}, \epsilon)} \|H_i(\mathbf{x}')\|_2$ .

The detailed proofs and the similar bounds of the local top- $k$  ranking thickness are in Appendix A.1. The bounds have the following implications and interpretations.

- The bounds of  $\Theta$  are related to  $\mathbf{x}$ , not  $\mathbf{x}'$ . Thus, optimizing the lower bound requires  $M_1 \times M_2$  fewer times of backward propagations by freeing from the heavy computation in Eq. (3).
- The bounds are related to the perturbation budget  $\epsilon$ , but not to the distribution  $\mathcal{D}$ . Thus, Eq. (5) is valid for adversarial sample  $\mathbf{x}'$  (Yang et al., 2020a) with  $\|\delta\|_2 \leq \epsilon$  or any random distribution such as  $U(\mathbf{x}, \epsilon)$  (Wang et al., 2020c).
- We reveal another motivation for minimizing Hessian norm: rather than smoothing the curvature, we aim to tighten the bounds of thickness and to ultimately maximize the thickness without dealing with neighbor sampling and line integration in Eq. (3). In particular, as  $\|H(\mathbf{x})\|_2 \rightarrow 0$ , we have  $L_i + L_j \rightarrow 0$ ,  $\|H_i(\mathbf{x}) - H_j(\mathbf{x})\|_2 \rightarrow 0$ , and  $\lim_{\|H(\mathbf{x})\|_2 \rightarrow 0} \mathbb{E}_{\mathbf{x}'} \left[ \int_0^1 h(\mathbf{x}(t), i, j) dt \right] = h(\mathbf{x}, i, j)$ .
- The bounds are related to  $h(\mathbf{x}, i, j) = \mathcal{I}_i(\mathbf{x}) - \mathcal{I}_j(\mathbf{x})$  and the Hessian of  $f$ . Thus, *only* minimizing a Hessian norm (Dombrowski et al., 2019; 2021; Wang et al., 2020c) is insufficient for ranking explanation robustness (see Table 1).
- Authors in (Hein & Andriushchenko, 2017) connect the robustness of prediction  $f_c$  to the ratio  $\max_j \frac{f_c(\mathbf{x}) - f_j(\mathbf{x})}{\|\mathcal{I}(\mathbf{x}', c) - \mathcal{I}(\mathbf{x}', j)\|_2}$ , where the ratio stems from the *optimal* perturbation direction. Although we can adopt their proof to obtain a similar ratio  $\frac{\mathcal{I}_i(\mathbf{x}) - \mathcal{I}_j(\mathbf{x})}{\|\nabla \mathcal{I}_i(\mathbf{x}') - \nabla \mathcal{I}_j(\mathbf{x}')\|_2}$ , our experiments show that the second-order term in the denominator makes the optimization less stable and the training can hardly converge (see Table 5).

Based on Prop. 3.4, simultaneously maximizing the gap and minimizing Hessian norm improve the thickness. Thus, we

have the following optimization problem for robust feature ranking explanations:

$$\min_{\mathbf{w}} \mathcal{L}_{total}(f) = \mathcal{L}_{cls}(f) - \lambda_1 \mathbb{E}_{\mathbf{x}} \left[ \sum_{i=1}^k \sum_{j=k+1}^n h(\mathbf{x}, i, j) \right] + \lambda_2 \mathbb{E}_{\mathbf{x}} [\|H(\mathbf{x})\|_2], \quad (6)$$

where  $\lambda_1, \lambda_2 \geq 0$ . In this way, we optimize the gap and Hessian norm concentrating on  $\mathbf{x} \in \mathcal{X}_T$  and are free from expensive sampling. When  $\lambda_1 = 0$ , we recover Hessian norm minimization to smooth the curvature (Dombrowski et al., 2021). When  $\lambda_2 = 0$ , we only increase the gaps. We call the strategy that trains  $f$  using Eq. (6) *Robust Ranking Explanation via Thickness (R2ET)*.

**Connection to adversarial training (AT).** Prop. 3.5 shows that R2ET has the same effect as AT but uses regularizations to avoid intensive computations. Specifically, the bottleneck of AT is to find the optimal  $\delta$  for any  $\mathbf{x}$ , which makes AT  $M_1$  times more expensive than R2ET, where  $M_1$  is the number of attack iterations per  $\mathbf{x}$ . The proof shown in Appendix A.2 is based on the prior work (Xu et al., 2009).

**Proposition 3.5.** *The optimization problem in Eq. (6) is equivalent to the following min-max problem:*

$$\min_{\mathbf{w}} \max_{(\delta_{1,k+1}, \dots, \delta_{k,n}) \in \mathcal{N}} \mathcal{L}_{cls} - \mathbb{E}_{\mathbf{x}} \left[ \sum_{i=1}^k \sum_{j=k+1}^n h(\mathbf{x} + \delta_{i,j}, i, j) \right], \quad (7)$$

where  $\delta_{i,j} \in \mathbb{R}^n$  is a perturbation to  $\mathbf{x}$  targeting at the  $(i, j)$  pair of features.  $\mathcal{N}$  is the feasible set of perturbations where each  $\delta_{i,j}$  is independent of each other, with  $\|\sum_{i,j} \delta_{i,j}\| \leq \epsilon$

**Acceleration.** Usually many non-salient features are less likely to be confused with the top- $k$  salient features (see Fig. 9), and we expedite R2ET by comparing fewer pairs. Specifically, we approximate the top- $k$  ranking thickness by  $k'$  pairs of features  $\sum_{i=1}^{k'} h(\mathbf{x}, k-i, k+i)$  with  $\mathcal{O}(k')$  complexity. When  $k' = k$ , we preserve the relative rankings of the top- $2k$  features, which is named **R2ET-mm**.

## 4. Analyses of numerical and statistical robustness

**Numerical stability of explanations.** We analyze how maximizing the thickness can improve explanation robustness under adversarial attacks. Different from prior work, we characterize the worst-case complexity of explanation robustness using iterative numerical algorithm for constrained multi-objective optimization. *Threat model.* Given the model  $f$ , an input  $\mathbf{x}$ , and an initial feature ranking, the attacker aims to swap the ranking of any pair of a salient feature  $i$  and a non-salient feature  $j$ , so that the gap  $h(\mathbf{x}, i, j) < 0$ . The attacker is constrained to neither

change the input  $\mathbf{x}$  nor the predictions  $f(\mathbf{x})$  significantly for stealthiness. Figure 7 in the Appendix shows that such constraints make the attack more challenging. We assume that the attacker has access to the parameters and architecture of the model  $f$  to conduct gradient-based white-box attacks, which are stronger than black-box attacks, as we do not have the sign of obfuscated gradients (Athalye et al., 2018) (see Figure 2).

**Optimization problem for the attack.** Each  $h(\mathbf{x}, i, j)$  can be treated as an objective function for the attacker, who however does not know which objective is the easiest to attack. Furthermore, attacking one objective can make another easier or harder to attack due to their dependency on the same model  $f$  and the input  $\mathbf{x}$ . As a result, an attack against a specific target feature pair does not reveal the true robustness of the feature ranking. We quantify the hardness of a successful attack (equivalently, explanation robustness) by an upper bound on the number of iterations for the attacker to flip the *first* (unknown) feature pair. The longer it takes to flip the first pair, the more robust the explanations of  $f(\mathbf{x})$  are. Formally, for any given initial input  $\mathbf{x}^{(0)}$  ( $k$  in the superscript means the  $k$ -th attacking iteration), the attacker needs to iteratively manipulate  $\mathbf{x}$  to reduce the gaps  $h(\mathbf{x}, i, j)$  for all  $i \in \{1, \dots, k\}$  and  $j \in \{k+1, \dots, n\}$  packed in a vector objective function:

$$\text{MOO-Attack}(\mathbf{x}, \epsilon) \quad \begin{cases} \min_{\mathbf{x}} & [h_1(\mathbf{x}), \dots, h_\ell(\mathbf{x}), \dots, h_m(\mathbf{x})], \\ \text{s.t.} & \|f(\mathbf{x}) - f(\mathbf{x}^{(0)})\| \leq \epsilon, \end{cases} \quad (8)$$

with  $h_\ell(\mathbf{x}) \stackrel{\text{def}}{=} h(\mathbf{x}, i, j)$ , with  $\ell = 1, \dots, m$  indexing the  $m$  pairs of  $(i, j)$ .

*Comments:* (i) the scalar function  $\sum_i \sum_j h(\mathbf{x}, i, j)$  is unsuitable for theoretical analyses, since there can be no pair of features flipped at a stationary point of the sum. Simultaneously minimizing multiple objectives allows us to determine when the first pair of features is flipped and gives a pessimistic bound for the defender (and thus an optimistic bound for the attacker). Empirically, minimizing  $\sum_i \sum_j h(\mathbf{x}, i, j)$  suffices to attack some explanations. (ii) We could have adopted the Pareto criticality for convergence analysis as in (Fliege & Vaz, 2016), but a Pareto critical point indicates that no critical direction (moving in which does not violate the constraint) leads to a joint descent in *all* objectives, rather than that an objective function  $h_\ell$  has been sufficiently minimized. (iii) Different from the local convergence results in (Fliege & Svaiter, 2000), we provide a global rate of convergence that justifies thickness maximization, and different from the unconstrained case in (Fliege et al., 2019), we constrain the amount of changes in  $\mathbf{x}$  and  $f(\mathbf{x})$ .

We propose a trust-region method Algorithm 1 in the Appendix to solve MOO-Attack( $\mathbf{x}, \epsilon$ ). If the algorithm reaches a critical point (where at least one objective function can-

not be reduced) without flipping any pair of features, the objective function(s) that cannot be further reduced will be removed from the objective vector of MOO-Attack( $\mathbf{x}$ ,  $\epsilon$ ) and Algorithm 1 will run on the remaining objectives. Since it takes a bounded number of iterations to reach a critical point (Theorem 4.1) and the objective functions are monotonically decreasing after each run of the algorithm (Lemma A.8), the number of iterations for an attacker to flip a pair of features, or to claim that the attack fails, is bounded by  $\lceil m(h_{\text{up}} - h_{\text{low}}) \frac{\kappa}{\epsilon^2} \rceil$ , where  $m$  is the number of objectives,  $h_{\text{up}} - h_{\text{low}}$  is the distance between the maximum of any  $h_\ell$  and the minimum of any  $h_\ell$ ,  $\kappa$  is a constant depending the parameters of the trust-region method and the smoothness of the objective and constraint functions, and  $\epsilon$  is the tolerance of optimization accuracy.

Technically, for each objective function  $h_\ell(\mathbf{x})$  and a scalar target  $t \in \mathbb{R}$ , define the merit function  $\phi_\ell$  that combines the  $\ell$ -th objective and the constraint in Eq. (8):

$$\phi_\ell(x, t) \stackrel{\text{def}}{=} \|f(\mathbf{x})\| + |h_\ell(\mathbf{x}) - t|. \quad (9)$$

Lemma A.5 in the Appendix shows these merit functions will remain small while the targets  $t$ , and thus  $h_\ell$ , can be jointly minimized. As an approximating model for the trust-region method, define the linearization of  $\phi(\mathbf{x}, t)$  as

$$l_{\phi_\ell}(\mathbf{x}, t, \mathbf{d}) = \|f(\mathbf{x}) + J(\mathbf{x})^\top \mathbf{d}\| + |h_\ell(\mathbf{x}) + g_\ell(\mathbf{x})^\top \mathbf{d} - t|,$$

where  $J(\mathbf{x})$  is the Jacobian of  $f$  at  $\mathbf{x}$  and  $g_\ell(\mathbf{x})$  is the gradient of  $h_\ell$  at  $\mathbf{x}$ . The maximal reduction in  $l_{\phi_\ell}(\mathbf{x}, t, 0)$  within a radius of  $\Delta > 0$  at  $\mathbf{x}$  is

$$\chi_\ell(\mathbf{x}, t) \stackrel{\text{def}}{=} l_{\phi_\ell}(\mathbf{x}, t, 0) - \min_{\mathbf{d}: \|\mathbf{d}\| \leq \Delta} l_{\phi_\ell}(\mathbf{x}, t, \mathbf{d}). \quad (10)$$

When  $\chi_\ell(\mathbf{x}, t) = 0$  (or  $\leq \epsilon$ ),  $\mathbf{x}$  is a critical (approximately critical) point of  $\phi_\ell$ .

The core of Algorithm 1 is the following optimization problem, TR-MOO( $\mathbf{x}$ ,  $\Delta$ ), whose optimal solution provides a descent direction  $\mathbf{d}$  for all  $l_{\phi_\ell}$  (not  $h_\ell$  or  $\phi_\ell$ ):

$$\text{TR-MOO}(\mathbf{x}, \Delta) \quad \begin{cases} \min_{\alpha, \mathbf{d}} & \alpha \\ \text{s.t.} & l_{\phi_\ell}(\mathbf{x}, t, \mathbf{d}) \leq \alpha, \ell = 1, \dots, m, \\ & \|\mathbf{d}\| \leq \Delta. \end{cases}$$

where  $\alpha$  is the minimal amount of descent and  $\Delta$  is the current radius of search for  $\mathbf{d}$ . With details in the Appendix, we show the following convergence result:

**Theorem 4.1.** *Suppose assumptions H.1-H.3 in the Appendix hold. Then Algorithm 1 generates an  $\epsilon$ -first-order critical point for problem Eq. (27) in at most  $\lceil (h_{\text{up}} - h_{\text{low}}) \frac{\kappa}{\epsilon^2} \rceil$  iterations, where  $\kappa$  is a constant independent of  $\epsilon$  but depending on the parameters  $\gamma$  and  $\eta$  of the trust-region method, and the global Lipschitz constants  $L_J$  of the Jacobian  $J$  and  $L_{g_\ell}$  of the gradients  $g_\ell$ .*

**Statistical stability of explanations.** We utilize a McDairmid’s inequality for dependent random variables and covering number of the space  $\mathcal{F}$  of saliency maps to show a bound on how likely R2ET can rank some non-salient features higher than some salient features due to perturbation to  $\mathbf{x}$ .

**Theorem 4.2.** *Given prediction model  $f$ , input  $\mathbf{x}$ , surrogate loss  $\phi_u$ , and a constant  $\epsilon > 0$ , for arbitrary saliency map  $\mathcal{I} \in \mathcal{F}$  and any distribution  $\mathcal{D}$  surrounding  $\mathbf{x}$  that preserves the salient features in  $\mathbf{x}$ , we have*

$$\begin{aligned} \Pr_{\mathbf{x}' \sim \mathcal{D}} \{ R_{0,1}^{\text{true}}(\mathcal{I}, \mathbf{x}') \geq R_{0,1,u}^{\text{emp}}(\mathcal{I}, \mathbf{x}) + \epsilon \} \\ \leq 2\mathcal{N}(\mathcal{F}, \frac{\epsilon u}{8}) \exp\left(-\frac{2m\epsilon^2}{\chi}\right), \end{aligned} \quad (11)$$

where  $\mathcal{N}(\mathcal{F}, \frac{\epsilon u}{8})$  is the covering number of the functional space  $\mathcal{F}$  with radius  $\frac{\epsilon u}{8}$  (Zhang, 2002).

$\chi >$  is the chromatic number of a dependency graph of all pairs of salient and non-salient features (Usunier et al., 2005) when applying the McDairmid’s inequality. The constant  $u > 0$  represents the required gap between  $\mathcal{I}_i(\mathbf{x})$  and  $\mathcal{I}_j(\mathbf{x})$ . For the details of relevant definitions and a sketch of proof, see Appendix A.4.

## 5. Experiments

Appendix B provides more comprehensive details and experimental results, including the reproducibility checklist, sensitivity analysis. and explanation faithfulness evaluation.

**Model architectures and datasets.** We adopt single-input DNN for three tabular datasets: Bank (Moro et al., 2014), Adult, and COMPAS (Mothilal et al., 2020), and an image dataset CIFAR-10 (Krizhevsky et al., 2009). We also evaluate two-input Siamese networks on an image dataset MNIST (LeCun et al., 1998) and two graph datasets: BP (Ma et al., 2019) and ADHD (Ma et al., 2016).

**Evaluation metrics.** We use Precision@ $k$  (P@ $k$ ) (Ghorbani et al., 2019; Wang et al., 2020c) to quantify the similarity between explanations before and after attacks. To ensure all the trained models have similarly good prediction performance, we report clean AUC, adversarial AUC, and sensitivity in B.6.4 and B.6.5. Besides, we adopt three faithfulness metrics (Serrano & Smith, 2019; DeYoung et al., 2019) in B.8 to show that explanations from R2ET are faithful.

**Explanation methods.** We adopt SimpleGrad as explanation method. Results for SmoothGrad (Smilkov et al., 2017) and IG (Sundararajan et al., 2017) are reported in B.7, where similar conclusions to SimpleGrad can be drawn.

## 5.1. Compared Methods

We conduct two attacks in the PGD manner (Madry et al., 2017): Explanation Ranking attack (ERAttack) and MSE attack. ERAttack minimizes  $\sum_{i=1}^k \sum_{j=k+1}^n h(\mathbf{x}', i, j)$  to manipulate the ranking of features in explanation  $\mathcal{I}(\mathbf{x})$ , and MSE attack maximizes the MSE (i.e.,  $\ell_2$  distance) between  $\mathcal{I}(\mathbf{x})$  and  $\mathcal{I}(\mathbf{x}')$ . We compare the proposed defense strategy R2ET with the following baselines.

- **Vanilla**: provides the basic ReLU model trained without weight decay or any regularizer term.
- **Weight decay (WD) (Dombrowski et al., 2021)**: uses weight decay during training to bound Hessian norm.
- **Softplus (SP) (Dombrowski et al., 2019; 2021)**: replaces ReLU with Softplus( $x; \rho$ ) =  $\frac{1}{\rho} \ln(1 + e^{\rho x})$ .
- **Estimated-Hessian (Est-H) (Dombrowski et al., 2021)**: adds Hessian norm as the regularizer, which is estimated by the finite difference (Moosavi-Dezfooli et al., 2019):  $\left\| \frac{\nabla f(\mathbf{x} + \kappa \mathbf{v}) - \nabla f(\mathbf{x})}{\kappa} \right\|_2$ , where  $\kappa \ll 1$ ,  $\mathbf{v} = \frac{\text{sign}(\nabla f(\mathbf{x}))}{\|\text{sign}(\nabla f(\mathbf{x}))\|_2}$ . It can be considered an ablation variant of R2ET ( $\lambda_1 = 0$ ).
- **Exact-Hessian (Exact-H)**: uses the exact Hessian norm as the regularizer.
- **SSR (Wang et al., 2020c)**: sets the largest eigenvalue of the Hessian matrix as the regularizer.
- **Adversarial Training (AT) (Huang et al., 2016; Wong et al., 2020)**: finds  $f$  by  $\min_f \sum_{(\mathbf{x}, y) \in (\mathcal{X}_T, \mathcal{Y}_T)} (\mathcal{L}_{cls}(f; \mathbf{x} + \delta^*, y))$ , where  $\delta^* = \arg \max_{\delta} - \sum_{i=1}^k \sum_{j=k+1}^n h(\mathbf{x} + \delta, i, j)$ .
- **R2ET-mm**: selects *multiple* distinct  $i, j$  with *minimal*  $h(\mathbf{x}, i, j)$  as discussed in Sec. 3.2.
- **R2ET $\setminus$ H** and **R2ET-mm $\setminus$ H**: They are the ablation variants of R2ET and R2ET-mm, respectively, without optimizing the Hessian-related term in Eq. (6) ( $\lambda_2 = 0$ ).

## 5.2. Overall robustness results

**Attackability of ranking-based explanation.** Table 1 reports P@k under ERAttack and MSE attacks for every model on all datasets. We observe that more than 50% of models achieve at least 90% P@k under MSE attacks, concluding that MSE attack cannot effectively alter the rankings of salient features, even without extra defense (row Vanilla). The ineffective attack method can give a false impression of explanation robustness. In contrast, ERAttack can displace more salient features from the top-k positions for most models and datasets, leading to significantly lower P@k values than MSE attack. For example, about 50% of the top 50 features are out of top positions under ERAttack on average on ADHD, while less than 20% of the top 50 features drop

out of the top under the MSE attack. The trade-off between accuracy and explanation robustness is explored in Fig. 8.

## Effectiveness of ranking thickness against ERAttacks.

We evaluate the effectiveness of different defense strategies against ERAttack, and similar conclusions can be made with MSE attacks case. (1) R2ET and its variants achieve the best (highest) top-k explanation robustness for most datasets, indicating their superiority in preserving the top salient features. (2) It is counter-intuitive that R2ET $\setminus$ H, as an ablation version of R2ET, outperforms R2ET on Adult and Bank. The reason is that R2ET $\setminus$ H has a better ranking thickness on these datasets than R2ET (see Fig. 2 in Sec. 5.3). (3) Overall, the baselines that strive for a smoother curvature without considering the gaps among feature importance, including WD, SP, Est-H, Exact-H, and SSR, performs unstably and usually badly across datasets. Moreover, bad performance of Est-H, Exact-H, and SSR, which smooth the curvature by adding Hessian-related terms, is consistent with the discussion in Sec 3.2. Specifically, minimizing Hessian norm helps tighten the bounds, while *solely* optimizing Hessian norm may marginally contribute to the ranking robustness. Since it is extremely expensive to compute the exact Hessian and its eigenvalues, Exact-H and SSR only apply to tabular datasets. (4) We do not compare with many AT baselines (Wang et al., 2012; Ivankay et al., 2020; Singh et al., 2020; Wang & Kong, 2022; Sarkar et al., 2021) due to their time-consuming nature. We adopt “fast”-AT (Wong et al., 2020) for AT baseline, where the inner maximization is solved by a single-step attack to balance the training time and robust performance. However, “Fast”-AT suffers from unstable robust performance as studied in (Li et al., 2020), and cannot perform well on most datasets.

## 5.3. Analysis on Explanation Ranking Thickness and Existing Metric

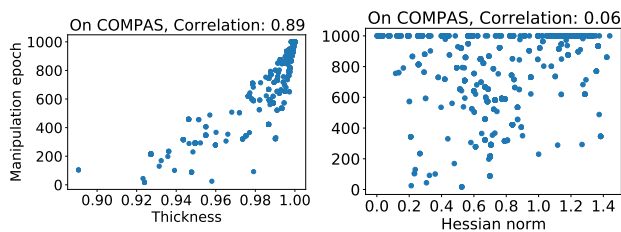
As shown in Table 1, R2ET and its variants are the winners on almost all the datasets except COMPAS and BP, and R2ET $\setminus$ H and R2ET-mm $\setminus$ H outperform their counterparts (R2ET and R2ET-mm) on Adult and Bank. We aim to identify the essential factor that helps a method outperform others.

As discussed in Sec. 4, the number of attack iterations to reach the first successful flip of a pair of salient and non-salient features characterizes the ranking explanation robustness. We show the correlations among the number of ERAttack iterations, Hessian norm, and thickness in the first two subplots in Fig. 2. Each dot in the subplots indicates one sample  $\mathbf{x}$ , and the correlation coefficient is reported. Compared with Hessian norm, thickness is significantly more correlated with the number of iterations to the first flip, and it indicates that thickness is a more fundamental measurement of ranking robustness, confirming the theoretical

## Provable Robust Saliency-based Explanations

Table 1:  $P@k$  (shown in percentage) of different robust models (rows) under **ERAttack / MSE attack**.  $k = 8$  for the first three dataset, and  $k = 50$  for the rest. Numbers in **bold** highlight the winner, and underlines indicate the runner-up. (\* Est-H has 4.6% and 3.9% lower clean AUC than R2ET-mm under two attacks, respectively.)

Method	Adult	Bank	COMPAS	MNIST	CIFAR-10	ADHD	BP
Vanilla	87.6 / 87.7	83.0 / 94.0	84.2 / 99.7	59.0 / 64.0	66.5 / 68.3	45.5 / 81.1	69.4 / 88.9
WD	91.7 / 91.8	82.4 / 85.9	87.7 / 99.4	59.1 / 64.8	64.2 / 65.6	47.6 / 79.4	69.4 / 88.6
SP	<u>97.4 / 97.5</u>	95.4 / 95.5	<b>99.5 / 100.0</b>	62.9 / 66.9	67.2 / 71.9	42.5 / 81.3	68.7 / 90.1
Est-H	87.1 / 87.2	78.4 / 81.8	82.6 / 97.7	85.2 / 90.2	77.1 / 78.7	58.2 / 83.7	<b>75.0* / 91.4*</b>
Exact-H	89.6 / 89.7	81.9 / 85.6	77.2 / 96.0	- / -	- / -	- / -	- / -
SSR	91.2 / 92.6	76.3 / 84.5	82.1 / 97.2	- / -	- / -	- / -	- / -
AT	68.4 / 91.4	80.0 / 88.4	84.2 / 90.5	56.0 / 63.9	61.6 / 66.8	59.4 / 81.0	72.0 / 89.0
R2ET $\setminus_H$	<b>97.5 / 97.7</b>	<b>100.0 / 100.0</b>	91.0 / 99.2	82.8 / 89.7	67.3 / 72.2	60.7 / 86.8	70.9 / 89.5
R2ET-mm $\setminus_H$	93.5 / 93.6	<u>95.8 / 98.2</u>	<u>95.3 / 97.2</u>	81.6 / 89.7	<u>77.7 / 79.4</u>	<u>64.2 / 88.8</u>	72.4 / 91.0
R2ET	92.1 / 92.7	80.4 / 90.5	92.0 / <u>99.9</u>	<b>85.7 / 90.8</b>	75.0 / 77.4	<b>71.6 / 91.3</b>	71.5 / 89.9
R2ET-mm	87.8 / 87.9	75.1 / 85.4	82.1 / 98.4	<u>85.3 / 91.4</u>	<b>78.0 / 79.1</b>	58.8 / 87.5	<u>73.8 / 91.1</u>



Method	Adult	COMPAS	BP
SP	97.4 / 0.9983	<b>99.5 / 0.9999</b>	68.7 / 0.9300
Est-H	87.1 / 0.9875	82.6 / 0.9557	<b>75.0 / 0.93563</b>
R2ET $\setminus_H$	<b>97.5 / 0.9989</b>	91.0 / 0.9727	70.9 / 0.9271
R2ET	92.1 / 0.9970	<u>92.0 / 0.9865</u>	71.5 / 0.9296
R2ET-mm	87.8 / 0.9943	82.1 / 0.9544	<u>73.8 / 0.93561</u>

Figure 2: Correlation between the number of iterations to first flip, and *sample-level* thickness (left) and Hessian norm (middle) for R2ET model on COMPAS. Correction between  $P@k$  and *model-level* thickness (right).

analysis in Sec. 4. Now we explain why R2ET cannot consistently outperform others. The table in Fig. 2 reports the *model-level* thickness by averaging sample thickness over the dataset. We attribute R2ET’s lack of top performance to its thickness, since the model with best explanation robustness ( $P@k$ ) consistently has the highest thickness. See Fig. 5 and Table 2 in B.6.2 for more results of *sample-level* and *model-level* thickness, respectively.

### 5.4. Case study: saliency maps visualization

MNIST and CIFAR-10 provide suitable testbeds for visual evaluation. In Fig. 3, we conduct ERAttack against models trained with different strategies. On MNIST, Vanilla and WD perform poorly, where about 30% ~ 60% of the top 50 important pixels fell out of top positions under ERAttack. Even worse, the top 50 salient pixels used by Vanilla and WD do not highlight the spatial patterns of the digits (e.g., pixels covering the digits). For R2ET and R2ET-mm, it is hard to find visible change in the top salient pixels before and after ERAttack, and  $P@k$  of both methods are greater than 90%. Besides, the top 50 important pixels used by

R2ET and R2ET-mm encode recognizable spatial patterns of the digits. We have similar conclusions on CIFAR-10. Specifically, we take the explanations on the ship in Fig. 3 bottom as an example. Vanilla and WD perform badly regarding  $P@k$ , while R2ET and R2ET-mm achieve around as high as 90%  $P@k$ . All four models make correct predictions due to a similar region (front hull of the ship). However, ERAttack manipulates the explanations of Vanilla and WD to include another region (wheelhouse of the ship), while the critical regions in the explanations of R2ET and R2ET-mm under attacks remain the same. The wheelhouse may be one reason for classifying the image to ship, but the inconsistency of explanations due to imperceptible perturbations raises confusion and mistrust. See Fig. 6 for more results.

## 6. Related Work

**Explainable machine learning and explanation robustness.** Recent post-hoc explanation methods for deep networks can be categorized into gradient-based (Zhou et al., 2016; Selvaraju et al., 2017; Baldassarre & Azizpour, 2019; Smilkov et al., 2017; Sundararajan et al., 2017; Shrikumar et al., 2017), surrogate model based (Ribeiro et al., 2016; Huang et al., 2022; Vu & Thai, 2020), Shapley values (Lundberg & Lee, 2017; Chen et al., 2019a; Liu et al., 2020; Yuan et al., 2021; Ancona et al., 2019), and causality (Pearl, 2018; Chattopadhyay et al., 2019; Parafita & Vtrià, 2019). Although gradient-based methods are widely used (Nielsen et al., 2022), they are found to lack robustness against small perturbations (Ghorbani et al., 2019; Heo et al., 2019). Some works (Chen et al., 2019b; Singh et al., 2020; Ivankay et al., 2020; Wang & Kong, 2022; Sarkar et al., 2021; Upadhyay et al., 2021) propose to improve the explanation robustness by adversarial training (AT). To bypass the high time complexity of AT, some works propose replacing ReLU function with softplus (Dombrowski et al., 2021), training with weight decay (Dombrowski et al., 2019), and incorporating gradient- and Hessian-related terms as regularizers

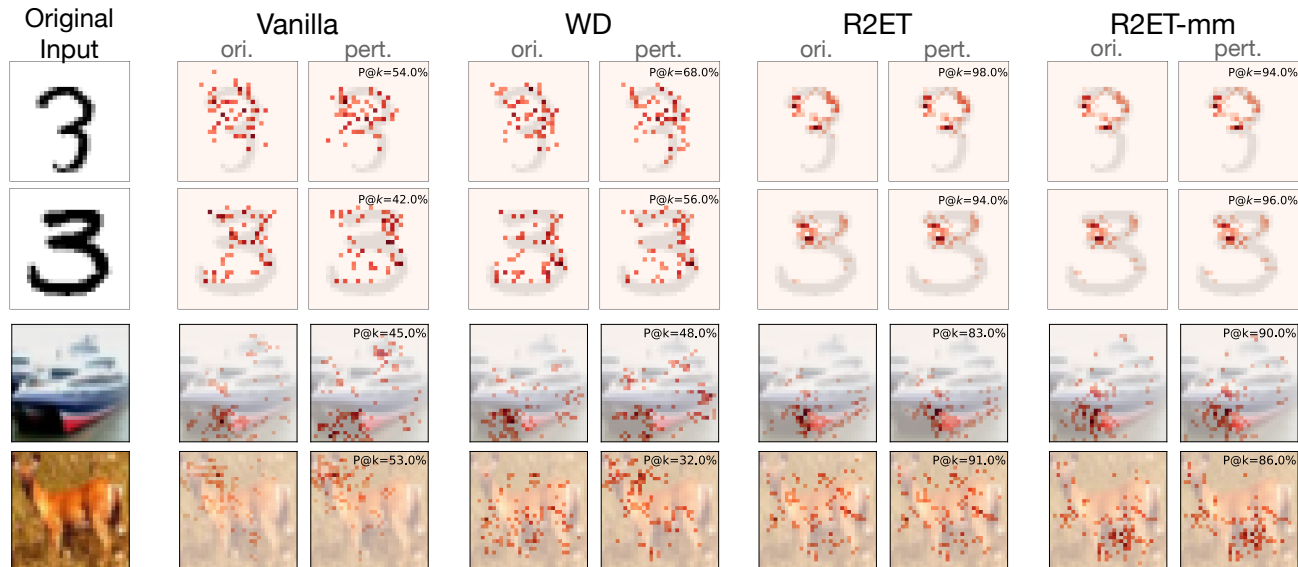


Figure 3: **Top**: With the Siamese network that compares two images from MNIST, saliency maps for the original and perturbed pairs of input images under ERAttack against different robust methods. The examples of a pair of images are from the same class (digit 3). **Bottom**: Explanations of ResNets concerning two images from CIFAR-10, one from class *ship* and another from class *deer*. The top  $k$  (50 for MNIST and 100 for CIFAR-10) salient pixels are highlighted, and darker colors indicate higher importance.  $P@k$  is reported within each subplot.

(Dombrowski et al., 2021; Wang et al., 2020c; Wicker et al., 2023). Some works propose *explanation* methods, rather than *training* methods, to enhance explanation robustness (Smilkov et al., 2017; Lu et al., 2021; Liu et al., 2022; Chen et al., 2021; Manupriya et al., 2022; Rieger & Hansen, 2020). Besides, many works (Madry et al., 2017; Tu et al., 2019; Wang et al., 2021; Moosavi-Dezfooli et al., 2019; Roth et al., 2020; Raghunathan et al., 2020; Yang et al., 2020a; Hein & Andriushchenko, 2017; Yang et al., 2020b; Deng et al., 2021; Tsipras et al., 2018; Wen et al., 2020; Zhang et al., 2019; Dominguez-Olmedo et al., 2022) for adversarial robustness focus on *prediction* robustness, instead of *explanation* robustness.

**Ranking robustness in IR.** Ranking robustness in information retrieval (IR) concerning noise (Zhou & Croft, 2006) and adversarial attacks (Goren et al., 2018; Zhou et al., 2020; 2021; Li et al., 2021; Wang et al., 2020a) is well-studied. Ranking manipulations in IR and explanations are different because 1) In IR, authors either manipulate the position of *one* candidate (Zhou et al., 2020; Goren et al., 2018), or manipulate a query to distort the ranking of candidates (Zhou et al., 2020; 2021; Li et al., 2021). We manipulate input to swap *any* pairs of salient and non-salient features. 2) Ranking in IR is based on the model predictions. However, explanations are defined by gradient or its variants, and studying their robustness requires second or higher-order derivatives, and it motivates us to design a surrogate regularizer to bypass costly computations.

**Top- $k$  intersection.** Top- $k$  intersection is widely used to

evaluate explanation robustness (Chen et al., 2019b; Wang et al., 2020c; Singh et al., 2020; Ivankay et al., 2020; Wang & Kong, 2022; Sarkar et al., 2021; Ghorbani et al., 2019). However, most existing works study the explanation robustness through  $\ell_p$  norm (Chen et al., 2019b; Dombrowski et al., 2019; 2021; Wang et al., 2020c), cosine similarity (Wang & Kong, 2022; 2023), Pearson correlation (Ivankay et al., 2020), Kendall tau (Wang & Kong, 2022), or KL-divergence (Sarkar et al., 2021). These correlations measure the explanation similarity using *all* features, and a high similarity can have entirely different top salient features. To optimize top- $k$  intersection in *classification* tasks, some works propose surrogate losses based on the upper bounds for top- $k$  intersection (Agarwal, 2011; Lapin et al., 2015; 2016; 2017; Berrada et al., 2018; Yang & Koyejo, 2020; Petersen et al., 2022). The upper bounds hold for predictions whose gaps are not larger than one, while it is not true for gradient-based explanations with unbounded values, making them unsuitable for *explanation* tasks.

## 7. Conclusion

We demonstrate that the ranking of explanations is more consistent with human intuition, and propose *explanation ranking thickness* to measure the ranking robustness quantitatively. To avoid the expensive neighbors sampling and adversarial training, we propose R2ET, which adopts the surrogate bounds of the thickness as regularization, to efficiently train ranking robust models. We further confirm that the thickness can be measured by the proposed thickness

metric by analyzing the convergence of the gradient-based attacks and experimental results. Even though we show the close correlation between thickness and explanation robustness, we cannot directly optimize the thickness as part of objective functions for robust training. Consequently, R2ET does not necessarily have the highest thickness, thus cannot consistently outperform other baselines.

## References

- Adebayo, J., Gilmer, J., Muelly, M., Goodfellow, I., Hardt, M., and Kim, B. Sanity checks for saliency maps. *NeurIPS*, 31, 2018.
- Agarwal, S. The infinite push: A new support vector ranking algorithm that directly optimizes accuracy at the absolute top of the list. In *SDM*, 2011.
- Ancona, M., Oztireli, C., and Gross, M. Explaining deep neural networks with a polynomial time algorithm for shapley value approximation. In *ICML*, 2019.
- Arora, S., Hazan, E., and Kale, S. The multiplicative weights update method: a meta-algorithm and applications. *Theory of Computing*, 2012.
- Athalye, A., Carlini, N., and Wagner, D. Obfuscated gradients give a false sense of security: Circumventing defenses to adversarial examples. In *ICML*, 2018.
- Baldassarre, F. and Azizpour, H. Explainability techniques for graph convolutional networks. *ICML*, 2019.
- Berrada, L., Zisserman, A., and Kumar, M. P. Smooth loss functions for deep top-k classification. *ICLR*, 2018.
- Boopathy, A., Liu, S., Zhang, G., Liu, C., Chen, P.-Y., Chang, S., and Daniel, L. Proper network interpretability helps adversarial robustness in classification. In *ICML*, 2020.
- Cartis, C., Gould, N. I. M., and Toint, P. L. On the complexity of finding first-order critical points in constrained nonlinear optimization. *Mathematical Programming*, 2014.
- Chattopadhyay, A., Manupriya, P., Sarkar, A., and Balasubramanian, V. N. Neural network attributions: A causal perspective. In *ICML*, 2019.
- Chen, C., Shen, Y., Ma, G., Kong, X., Rangarajan, S., Zhang, X., and Xie, S. Self-learn to explain siamese networks robustly. *ICDM*, 2021.
- Chen, J., Song, L., Wainwright, M. J., and Jordan, M. I. L-shapley and c-shapley: Efficient model interpretation for structured data. *ICLR*, 2019a.
- Chen, J., Wu, X., Rastogi, V., Liang, Y., and Jha, S. Robust attribution regularization. *NeurIPS*, 2019b.
- Deng, Z., Zhang, L., Ghorbani, A., and Zou, J. Improving adversarial robustness via unlabeled out-of-domain data. In *AISTATS*, 2021.
- DeYoung, J., Jain, S., Rajani, N. F., Lehman, E., Xiong, C., Socher, R., and Wallace, B. C. Eraser: A benchmark to evaluate rationalized nlp models. *ACL*, 2019.

- Dombrowski, A.-K., Alber, M., Anders, C. J., Ackermann, M., Müller, K.-R., and Kessel, P. Explanations can be manipulated and geometry is to blame. *NeurIPS*, 2019.
- Dombrowski, A.-K., Anders, C. J., Müller, K.-R., and Kessel, P. Towards robust explanations for deep neural networks. *Pattern Recognition*, 2021.
- Dominguez-Olmedo, R., Karimi, A. H., and Schölkopf, B. On the adversarial robustness of causal algorithmic recourse. In *ICML*, 2022.
- Fliege, J. and Svaiter, B. F. Steepest descent methods for multicriteria optimization. *Mathematical Methods of Operations Research*, 2000.
- Fliege, J. and Vaz, A. I. F. A method for constrained multiobjective optimization based on sqp techniques. *SIAM Journal on Optimization*, 2016.
- Fliege, J., Vaz, A. I. F., and Vicente, L. N. Complexity of gradient descent for multiobjective optimization. *Optimization Methods and Software*, 2019.
- Ghorbani, A., Abid, A., and Zou, J. Interpretation of neural networks is fragile. In *AAAI*, 2019.
- Goodman, B. and Flaxman, S. European union regulations on algorithmic decision-making and a “right to explanation”. *AI magazine*, 2017.
- Goren, G., Kurland, O., Tennenholtz, M., and Raiber, F. Ranking robustness under adversarial document manipulations. In *SIGIR*, 2018.
- He, K., Zhang, X., Ren, S., and Sun, J. Deep residual learning for image recognition. In *CVPR*, 2016.
- Hein, M. and Andriushchenko, M. Formal guarantees on the robustness of a classifier against adversarial manipulation. *NeurIPS*, 30, 2017.
- Heo, J., Joo, S., and Moon, T. Fooling neural network interpretations via adversarial model manipulation. *NeurIPS*, 2019.
- Huang, Q., Yamada, M., Tian, Y., Singh, D., and Chang, Y. Graphlime: Local interpretable model explanations for graph neural networks. *TKDE*, 2022.
- Huang, R., Xu, B., Schuurmans, D., and Szepesvári, C. Learning with a strong adversary. *ICLR*, 2016.
- Hudson, D. L. and Cohen, M. E. *Neural networks and artificial intelligence for biomedical engineering*. Wiley Online Library, 2000.
- Ivankay, A., Girardi, I., Marchiori, C., and Frossard, P. Far: A general framework for attributional robustness. *BMVC*, 2020.
- Krizhevsky, A., Hinton, G., et al. Learning multiple layers of features from tiny images. 2009.
- Lapin, M., Hein, M., and Schiele, B. Top-k multiclass svm. *NeurIPS*, 2015.
- Lapin, M., Hein, M., and Schiele, B. Loss functions for top-k error: Analysis and insights. In *CVPR*, 2016.
- Lapin, M., Hein, M., and Schiele, B. Analysis and optimization of loss functions for multiclass, top-k, and multilabel classification. *PAMI*, 2017.
- LeCun, Y., Bottou, L., Bengio, Y., and Haffner, P. Gradient-based learning applied to document recognition. *Proceedings of the IEEE*, 1998.
- Li, B., Wang, S., Jana, S., and Carin, L. Towards understanding fast adversarial training. *arXiv preprint arXiv:2006.03089*, 2020.
- Li, X., Li, J., Chen, Y., Ye, S., He, Y., Wang, S., Su, H., and Xue, H. Qair: Practical query-efficient black-box attacks for image retrieval. In *CVPR*, 2021.
- Lin, T., Jin, C., and Jordan, M. On gradient descent ascent for nonconvex-concave minimax problems. In *ICML*, 2020.
- Liu, A., Chen, X., Liu, S., Xia, L., and Gan, C. Certifiably robust interpretation via rényi differential privacy. *Artificial Intelligence*, 2022.
- Liu, Y., Chen, C., Liu, Y., Zhang, X., and Xie, S. Shapley values and meta-explanations for probabilistic graphical model inference. In *CIKM*, 2020.
- Lu, Y. Y., Guo, W., Xing, X., and Noble, W. S. Dance: Enhancing saliency maps using decoys. In *ICML*, 2021.
- Lundberg, S. M. and Lee, S.-I. A unified approach to interpreting model predictions. *NeurIPS*, 2017.
- Ma, G., He, L., Cao, B., Zhang, J., Yu, P. S., and Ragin, A. B. Multi-graph clustering based on interior-node topology with applications to brain networks. In *ECML PKDD*, 2016.
- Ma, G., Ahmed, N. K., Willke, T. L., Sengupta, D., Cole, M. W., Turk-Browne, N. B., and Yu, P. S. Deep graph similarity learning for brain data analysis. In *CIKM*, 2019.
- Madry, A., Makelov, A., Schmidt, L., Tsipras, D., and Vladu, A. Towards deep learning models resistant to adversarial attacks. *ICLR*, 2017.
- Manupriya, P., Menta, T. R., Jagarlapudi, S. N., and Balasubramanian, V. N. Improving attribution methods by learning submodular functions. In *AISTATS*, 2022.

- Moosavi-Dezfooli, S.-M., Fawzi, A., Uesato, J., and Frossard, P. Robustness via curvature regularization, and vice versa. In *CVPR*, 2019.
- Moro, S., Cortez, P., and Rita, P. A data-driven approach to predict the success of bank telemarketing. *Decision Support Systems*, 2014.
- Mothilal, R. K., Sharma, A., and Tan, C. Explaining machine learning classifiers through diverse counterfactual explanations. In *FAccT*, 2020.
- Nielsen, I. E., Dera, D., Rasool, G., Ramachandran, R. P., and Bouaynaya, N. C. Robust explainability: A tutorial on gradient-based attribution methods for deep neural networks. *IEEE Signal Processing Magazine*, 2022.
- Parafita, Á. and Vitrià, J. Explaining visual models by causal attribution. In *ICCVW*, 2019.
- Paulavičius, R. and Žilinskas, J. Analysis of different norms and corresponding lipschitz constants for global optimization. *Technol. Econ. Dev*, 2006.
- Pearl, J. Theoretical impediments to machine learning with seven sparks from the causal revolution. *WSDM*, 2018.
- Pearlmutter, B. A. Fast exact multiplication by the hessian. *Neural computation*, 1994.
- Petersen, F., Kuehne, H., Borgelt, C., and Deussen, O. Differentiable top-k classification learning. In *ICML*, 2022.
- Pu, P. and Chen, L. Trust building with explanation interfaces. In *IUI*, 2006.
- Raghunathan, A., Xie, S. M., Yang, F., Duchi, J., and Liang, P. Understanding and mitigating the tradeoff between robustness and accuracy. *ICML*, 2020.
- Ribeiro, M. T., Singh, S., and Guestrin, C. "why should i trust you?" explaining the predictions of any classifier. In *SIGKDD*, 2016.
- Rieger, L. and Hansen, L. K. A simple defense against adversarial attacks on heatmap explanations. *WHI*, 2020.
- Rieger, L., Singh, C., Murdoch, W., and Yu, B. Interpretations are useful: penalizing explanations to align neural networks with prior knowledge. In *ICML*, 2020.
- Rony, J., Granger, E., Pedersoli, M., and Ayed, I. B. Augmented lagrangian adversarial attacks. *ICCV*, 2020.
- Roth, K., Kilcher, Y., and Hofmann, T. Adversarial training is a form of data-dependent operator norm regularization. *NeurIPS*, 2020.
- Rudin, C. The P-Norm Push: A Simple Convex Ranking Algorithm That Concentrates at the Top of the List. *JMLR*, 2009.
- Saaty, T. L. and Ozdemir, M. S. Why the magic number seven plus or minus two. *Mathematical and computer modelling*, 2003.
- Sarkar, A., Sarkar, A., and Balasubramanian, V. N. Enhanced regularizers for attributional robustness. In *AAAI*, 2021.
- Selvaraju, R. R., Cogswell, M., Das, A., Vedantam, R., Parikh, D., and Batra, D. Grad-cam: Visual explanations from deep networks via gradient-based localization. In *ICCV*, 2017.
- Serrano, S. and Smith, N. A. Is attention interpretable? *ACL*, 2019.
- Shrikumar, A., Greenside, P., and Kundaje, A. Learning important features through propagating activation differences. In *ICML*, 2017.
- Singh, M., Kumari, N., Mangla, P., Sinha, A., Balasubramanian, V. N., and Krishnamurthy, B. Attributional robustness training using input-gradient spatial alignment. In *ECCV*, 2020.
- Smilkov, D., Thorat, N., Kim, B., Viégas, F., and Wattenberg, M. Smoothgrad: removing noise by adding noise. *arXiv preprint arXiv:1706.03825*, 2017.
- Sundararajan, M., Taly, A., and Yan, Q. Axiomatic attribution for deep networks. In *ICML*, 2017.
- Tsipras, D., Santurkar, S., Engstrom, L., Turner, A., and Madry, A. Robustness may be at odds with accuracy. *ICLR*, 2018.
- Tu, Z., Zhang, J., and Tao, D. Theoretical analysis of adversarial learning: A minimax approach. *NeurIPS*, 2019.
- Upadhyay, S., Joshi, S., and Lakkaraju, H. Towards robust and reliable algorithmic recourse. *NeurIPS*, 2021.
- Usunier, N., Amini, M. R., and Gallinari, P. Generalization error bounds for classifiers trained with interdependent data. In *NeurIPS*, 2005.
- Vu, M. and Thai, M. T. Pgm-explainer: Probabilistic graphical model explanations for graph neural networks. *NeurIPS*, 2020.
- Wang, F. and Kong, A. W.-K. Exploiting the relationship between kendall's rank correlation and cosine similarity for attribution protection. *NeurIPS*, 2022.
- Wang, F. and Kong, A. W.-K. A practical upper bound for the worst-case attribution deviations. *CVPR*, 2023.

- Wang, H., Wang, G., Li, Y., Zhang, D., and Lin, L. Transferable, controllable, and inconspicuous adversarial attacks on person re-identification with deep mis-ranking. In *CVPR*, 2020a.
- Wang, L., Bennett, P. N., and Collins-Thompson, K. Robust ranking models via risk-sensitive optimization. In *SIGIR*, 2012.
- Wang, W., Lesner, C., Ran, A., Rukonic, M., Xue, J., and Shiu, E. Using small business banking data for explainable credit risk scoring. In *AAAI*, 2020b.
- Wang, Y., Ma, X., Bailey, J., Yi, J., Zhou, B., and Gu, Q. On the convergence and robustness of adversarial training. *ICML*, 2021.
- Wang, Z., Wang, H., Ramkumar, S., Fredrikson, M., Mardziel, P., and Datta, A. Smoothed geometry for robust attribution. *NeurIPS*, 2020c.
- Wen, Y., Li, S., and Jia, K. Towards understanding the regularization of adversarial robustness on neural networks. In *ICML*, 2020.
- Wicker, M., Heo, J., Costabello, L., and Weller, A. Robust explanation constraints for neural networks. *ICLR*, 2023.
- Wong, E., Rice, L., and Kolter, J. Z. Fast is better than free: Revisiting adversarial training. *ICLR*, 2020.
- Xu, H., Caramanis, C., and Mannor, S. Robustness and regularization of support vector machines. *JMLR*, 2009.
- Xu, H., Ma, Y., Liu, H.-C., Deb, D., Liu, H., Tang, J.-L., and Jain, A. K. Adversarial attacks and defenses in images, graphs and text: A review. *Int. J. Autom. Comput.*, 2020.
- Yang, F. and Koyejo, S. On the consistency of top-k surrogate losses. In *ICML*, 2020.
- Yang, Y., Khanna, R., Yu, Y., Gholami, A., Keutzer, K., Gonzalez, J. E., Ramchandran, K., and Mahoney, M. W. Boundary thickness and robustness in learning models. *NeurIPS*, 2020a.
- Yang, Y.-Y., Rashtchian, C., Zhang, H., Salakhutdinov, R. R., and Chaudhuri, K. A closer look at accuracy vs. robustness. *NeurIPS*, 2020b.
- Yuan, H., Yu, H., Wang, J., Li, K., and Ji, S. On explainability of graph neural networks via subgraph explorations. In *ICML*, 2021.
- Zhang, H., Yu, Y., Jiao, J., Xing, E., El Ghaoui, L., and Jordan, M. Theoretically principled trade-off between robustness and accuracy. In *ICML*, 2019.
- Zhang, T. Covering Number Bounds of Certain Regularized Linear Function Classes. *JMLR*, 2002.
- Zhou, B., Khosla, A., Lapedriza, A., Oliva, A., and Torralba, A. Learning deep features for discriminative localization. In *CVPR*, 2016.
- Zhou, M., Niu, Z., Wang, L., Zhang, Q., and Hua, G. Adversarial ranking attack and defense. In *ECCV*, 2020.
- Zhou, M., Wang, L., Niu, Z., Zhang, Q., Xu, Y., Zheng, N., and Hua, G. Practical relative order attack in deep ranking. In *ICCV*, 2021.
- Zhou, Y. and Croft, W. B. Ranking robustness: a novel framework to predict query performance. In *CIKM*, 2006.

## A. Proofs

### A.1. Bounds of Ranking Explanation Thickness

In this section, we explore the lower and upper bounds of the ranking explanation thickness. We denote  $\mathbf{x}$  as the target sample,  $\|\delta\|_2 \leq \epsilon$  as the perturbation,  $\mathbf{x}' = \mathbf{x} + \delta$  as the perturbed input, and  $\mathbf{x}(t) = (1-t)\mathbf{x} + t\mathbf{x}'$ ,  $t \in [0, 1]$ .

**Proposition A.1** (Bounds of local ranking explanation thickness). *Given a  $L$ -locally Lipschitz model  $f(\mathbf{x})$ , for some  $L \geq \frac{\|\mathbf{x} - \mathbf{x}^*\|_2 \max_i L_i}{2}$  where  $\mathbf{x}^* = \arg \max_{\mathbf{x}' \in \mathcal{B}_2(\mathbf{x}, \epsilon)} \frac{\|\mathcal{I}(\mathbf{x}) - \mathcal{I}(\mathbf{x}')\|_2}{\|\mathbf{x} - \mathbf{x}'\|_2}$ , the local ranking explanation thickness for the  $(i, j)$  feature pair of a target  $\mathbf{x}$  is bounded by*

$$h(\mathbf{x}, i, j) - \epsilon * \frac{1}{2} \|H_i(\mathbf{x}) - H_j(\mathbf{x})\|_2 \leq \mathbb{E}_{\mathbf{x}'} \left[ \int_0^1 h(\mathbf{x}(t), i, j) dt \right] \leq h(\mathbf{x}, i, j) + \epsilon * (L_i + L_j),$$

where  $H_i(\mathbf{x})$  is the  $i$ -th column of Hessian matrix of  $f$  with respect to the input  $\mathbf{x}$ , and  $L_i = \max_{\mathbf{x}' \in \mathcal{B}_2(\mathbf{x}, \epsilon)} \|H_i(\mathbf{x}')\|_2$ .

**Lower bound.** We start from the definition of local ranking thickness between  $(i, j)$  pair of explanations of  $\mathbf{x}$  in Eq. (3).

$$\begin{aligned} & \int_0^1 h(\mathbf{x}(t), i, j) dt \\ &= \int_0^1 \mathcal{I}_i(\mathbf{x}(t)) - \mathcal{I}_j(\mathbf{x}(t)) dt \\ &= \int_0^1 \mathcal{I}_i(\mathbf{x} + t\delta) - \mathcal{I}_j(\mathbf{x} + t\delta) dt \\ &\approx \int_0^1 \mathcal{I}_i(\mathbf{x}) + t\delta^\top H_i(\mathbf{x}) - \mathcal{I}_j(\mathbf{x}) - t\delta^\top H_j(\mathbf{x}) dt \\ &= \mathcal{I}_i(\mathbf{x}) - \mathcal{I}_j(\mathbf{x}) + \frac{\delta^\top}{2} H_i(\mathbf{x}) - \frac{\delta^\top}{2} H_j(\mathbf{x}) \\ &\geq \mathcal{I}_i(\mathbf{x}) - \mathcal{I}_j(\mathbf{x}) - \epsilon * \frac{1}{2} \|H_i(\mathbf{x}) - H_j(\mathbf{x})\|_2, \end{aligned} \quad (12)$$

We approximate the gradient at intermediate point  $\mathbf{x} + t\delta$  by the Taylor Expansion on line-4. Then we find the minimum with  $\delta = \arg \min_{\|\delta\|_2 \leq \epsilon} \frac{1}{2} \delta^\top (H_i(\mathbf{x}) - H_j(\mathbf{x})) = -\epsilon \frac{H_i(\mathbf{x}) - H_j(\mathbf{x})}{\|H_i(\mathbf{x}) - H_j(\mathbf{x})\|_2}$  on line-6.

**Upper bound.** Before the proofs for the upper bound, we introduce two lemmas from (Paulavičius & Žilinskas, 2006) and (Wang et al., 2020c).

**Lemma A.2.** *If a function  $g : \mathbb{R}^n \rightarrow \mathbb{R}$  is  $L$ -locally Lipschitz within  $\mathcal{B}_p(\mathbf{x}, \epsilon)$ , such that  $|g(\mathbf{x}) - g(\mathbf{x}')| \leq L \|\mathbf{x} - \mathbf{x}'\|_p$ ,  $\forall \mathbf{x}' \in \mathcal{B}_p(\mathbf{x}, \epsilon) = \{\mathbf{x}' : \|\mathbf{x}' - \mathbf{x}\|_p \leq \epsilon\}$ , then*

$$L = \max_{\mathbf{x}' \in \mathcal{B}_p(\mathbf{x}, \epsilon)} \|\nabla_{\mathbf{x}'} g(\mathbf{x}')\|_q, \quad (13)$$

where  $\frac{1}{p} + \frac{1}{q} = 1$ ,  $1 \leq p, q \leq \infty$ .

**Lemma A.3.** *If a function  $f(\mathbf{x})$  is  $L$ -locally Lipschitz continuous in  $\mathcal{B}_2(\mathbf{x}, \epsilon)$ , then  $\mathcal{I}(\mathbf{x})$  is  $K$ -locally Lipschitz as well, where  $K \leq \frac{2L}{\|\mathbf{x} - \mathbf{x}^*\|}$  and  $\mathbf{x}^* = \arg \max_{\mathbf{x}' \in \mathcal{B}_2(\mathbf{x}, \epsilon)} \frac{\|\mathcal{I}(\mathbf{x}) - \mathcal{I}(\mathbf{x}')\|_2}{\|\mathbf{x} - \mathbf{x}'\|_2}$ .*

We now start our proofs from  $L$ -locally Lipschitz  $f(\mathbf{x})$ . Based on Lemma A.3 and Definition 3.3, we find that  $\forall i, \mathcal{I}_i(\mathbf{x}) : \mathbb{R}^n \rightarrow \mathbb{R}$ , any entry of  $\mathcal{I}(\mathbf{x})$ , is  $K$ -locally Lipschitz as well.

$$|\mathcal{I}_i(\mathbf{x}) - \mathcal{I}_i(\mathbf{x}')| \leq \|\mathcal{I}(\mathbf{x}) - \mathcal{I}(\mathbf{x}')\|_2 \leq K \|\mathbf{x} - \mathbf{x}'\|_2.$$

Specifically, we denote the locally Lipschitz constant for  $\mathcal{I}_i(\mathbf{x})$  as  $L_i \leq K$ , and based on Lemma A.2, we have  $L_i = \max_{\mathbf{x}' \in \mathcal{B}_2(\mathbf{x}, \epsilon)} \|\nabla_{\mathbf{x}'} \mathcal{I}_i(\mathbf{x}')\|_2 = \max_{\mathbf{x}' \in \mathcal{B}_2(\mathbf{x}, \epsilon)} \|H_i(\mathbf{x}')\|_2$  by taking  $p = q = 2$ .

$$\begin{aligned} & \int_0^1 h(\mathbf{x}(t), i, j) dt \\ &= h(\mathbf{x}'_0, i, j) \\ &= (\mathcal{I}_i(\mathbf{x}'_0) - \mathcal{I}_i(\mathbf{x})) - (\mathcal{I}_j(\mathbf{x}'_0) - \mathcal{I}_j(\mathbf{x})) + (\mathcal{I}_i(\mathbf{x}) - \mathcal{I}_j(\mathbf{x})) \\ &\leq |\mathcal{I}_i(\mathbf{x}'_0) - \mathcal{I}_i(\mathbf{x})| + |\mathcal{I}_j(\mathbf{x}'_0) - \mathcal{I}_j(\mathbf{x})| + (\mathcal{I}_i(\mathbf{x}) - \mathcal{I}_j(\mathbf{x})) \\ &\leq L_i \|\mathbf{x}'_0 - \mathbf{x}\|_2 + L_j \|\mathbf{x}'_0 - \mathbf{x}\|_2 + (\mathcal{I}_i(\mathbf{x}) - \mathcal{I}_j(\mathbf{x})) \\ &\leq \epsilon * (L_i + L_j) + (\mathcal{I}_i(\mathbf{x}) - \mathcal{I}_j(\mathbf{x})). \end{aligned} \quad (14)$$

Based on first mean value theorem, there exists a point  $\mathbf{x}'_0$  within the line segment  $\mathbf{x}$  and  $\mathbf{x}'$  such that  $h(\mathbf{x}'_0, i, j) = \int_0^1 h(\mathbf{x}(t), i, j) dt$  on line-2. The inequality on line-4 holds since  $\mathcal{I}_i(\mathbf{x}) : \mathbb{R}^n \rightarrow \mathbb{R}$  is a scalar function, and any scalar is less than or equivalent to its absolute value. The inequality on line-5 holds due to  $L_i$ -locally Lipschitz of  $\mathcal{I}_i(\mathbf{x})$  and Lemma A.2 with  $p = q = 2$ . The inequality on line-6 holds due to the fact that  $\mathbf{x}'_0$  locates within  $\mathcal{B}_2(\mathbf{x}, \epsilon)$ .

Now we look for the specific  $L$  for the upper bound. Notice that  $K \leq \frac{2L}{\|\mathbf{x} - \mathbf{x}^*\|}$  and  $L_i = \max_{\mathbf{x}' \in \mathcal{B}_2(\mathbf{x}, \epsilon)} \|H_i(\mathbf{x}')\|_2 \leq K$ , we have

$$\begin{aligned} L &\geq \frac{\|\mathbf{x} - \mathbf{x}^*\|}{2} * K \\ &\geq \frac{\|\mathbf{x} - \mathbf{x}^*\|}{2} * \max_i L_i \\ &= \frac{\|\mathbf{x} - \mathbf{x}^*\|}{2} * \max_i \max_{\mathbf{x}' \in \mathcal{B}_2(\mathbf{x}, \epsilon)} \|H_i(\mathbf{x}')\|_2. \end{aligned} \quad (15)$$

**Extension.** Notice that both the lower bound in Eq. (12) and the upper bounds in Eq. (14) hold for any choice of  $\mathbf{x}' \in \mathcal{B}_2(\mathbf{x}, \epsilon)$  with a specific  $\epsilon$ . Thus,

$$h(\mathbf{x}, i, j) - \epsilon * \frac{1}{2} \|H_i(\mathbf{x}) - H_j(\mathbf{x})\|_2 \leq \mathbb{E}_{\mathbf{x}'} \left[ \int_0^1 h(\mathbf{x}(t), i, j) dt \right] \leq h(\mathbf{x}, i, j) + \epsilon * (L_i + L_j).$$

Furthermore, the bounds of the relaxed local top- $k$  ranking thickness are

$$\begin{aligned}
 & \sum_{i=1}^k \sum_{j=k+1}^n \left[ h(\mathbf{x}, i, j) - \epsilon * \frac{1}{2} \|H_i(\mathbf{x}) - H_j(\mathbf{x})\|_2 \right] \\
 & \leq \mathbb{E}_{\mathbf{x}'} \left[ \sum_{i=1}^k \sum_{j=k+1}^n \int_0^1 h(\mathbf{x}(t), i, j) dt \right] \\
 & \leq \sum_{i=1}^k \sum_{j=k+1}^n [h(\mathbf{x}, i, j) + \epsilon * (L_i + L_j)].
 \end{aligned} \tag{16}$$

Even though one can broaden the thickness of *one*  $(i, j)$  pair by maximizing  $\mathcal{I}_i(\mathbf{x}) - \mathcal{I}_j(\mathbf{x})$  and minimizing  $\|H_i(\mathbf{x}) - H_j(\mathbf{x})\|_2$  explicitly, it is infeasible to minimize  $\|H_i(\mathbf{x}) - H_j(\mathbf{x})\|_2$  in the top- $k$  thickness case. Notice that  $H_i(\mathbf{x}) = H_j(\mathbf{x}), \forall i \in \{1, \dots, k\}, \forall j \in \{k+1, \dots, n\}$  indicates  $H_i(\mathbf{x}) = H_j(\mathbf{x}), \forall i, j \in \{1, \dots, n\}$ , and we have  $H_{iv}(\mathbf{x}) = H_{jv}(\mathbf{x})$  where  $H_{iv}(\mathbf{x})$  is the element in the  $i$ -th row and  $v$ -th column of the Hessian matrix. For any  $i, j, u, v \in \{1, \dots, n\}$ ,  $H_{iv}(\mathbf{x}) = H_{jv}(\mathbf{x}) = H_{vj}(\mathbf{x}) = H_{uj}(\mathbf{x})$  holds, which implies that *all* elements in the Hessian matrix of the optimum are the same and indicates zero determinant of  $H$ . An alternative practical objective is to minimize the Hessian norm,  $\|H(\mathbf{x})\|$ , to tighten the bounds of thickness.

## A.2. Connection between AT and R2ET

**Definition.** Following the notations used in Sec. 2, given a model  $f : \mathbb{R}^n \rightarrow [0, 1]^C$  and an input  $\mathbf{x}$ ,  $\mathcal{I}(\mathbf{x}, c; f) = \nabla_{\mathbf{x}} f_c(\mathbf{x})$  is the explanation and  $\mathcal{I}_i(\mathbf{x})$  is the feature score for the  $i$ -th feature. We further assume that  $\mathcal{I}(\mathbf{x})$  is sorted and top- $k$  ones are salient features.

The objective of Adversarial Training (AT) for training a model by a min-max game in Sec. 3.2 is:

$$\min_{\mathbf{w}} \max_{(\delta_{1,k+1}, \dots, \delta_{k,n}) \in \mathcal{N}} \mathcal{L}_{cls} - \mathbb{E}_{\mathbf{x}} \left[ \sum_{i=1}^k \sum_{j=k+1}^n h(\mathbf{x} + \delta_{i,j}, i, j) \right]. \tag{17}$$

We start with one training sample  $\mathbf{x}$ :

$$\min_{\mathbf{w}} \max_{(\delta_{1,k+1}, \dots, \delta_{k,n}) \in \mathcal{N}} \mathcal{L}_{cls} - \sum_{i=1}^k \sum_{j=k+1}^n h(\mathbf{x} + \delta_{i,j}, i, j). \tag{18}$$

For brevity, we consider an auxiliary label:  $l_i = 1$  for  $i \leq k$ , and  $l_i = -1$  otherwise. and re-write the goal of AT with the auxiliary label  $l_i$ :

$$\min_{\mathbf{w}} \max_{(\delta_1, \dots, \delta_m) \in \mathcal{N}} \mathcal{L}_{cls} - \sum_{i=1}^m l_i \mathcal{I}_i(\mathbf{x} + \delta_i), \tag{19}$$

or

$$\max_{\mathbf{w}} \min_{(\delta_1, \dots, \delta_m) \in \mathcal{N}} -\mathcal{L}_{cls} + \sum_{i=1}^m l_i \mathcal{I}_i(\mathbf{x} + \delta_i). \tag{20}$$

$m = k(n-k)$  and  $\delta_i$  is specific to the  $i$ -th feature of input  $\mathbf{x}$ . Based on the definition of  $l_i$ ,  $\sum_{i=1}^m l_i \mathcal{I}_i(\mathbf{x})$  shares the same goal as  $\sum_{i=1}^k \sum_{j=k+1}^n h(\mathbf{x}, i, j)$  but with different weights.

We will start with the inner  $(\delta)$  part in Eq. (20) to find the connection with R2ET. We define an  $\epsilon$  norm ball  $\mathcal{N}_0 \stackrel{\text{def}}{=} \{\delta : \|\delta\| \leq \epsilon\} \subseteq \mathbb{R}^n$ . We consider a perturbation set  $\mathcal{N} \subseteq \mathbb{R}^{n \times m}$  where the perturbations on *each feature* are independently, but the aggregation of perturbations is controlled. Formally,  $\mathcal{N}$  satisfies  $\mathcal{N}^- \subseteq \mathcal{N} \subseteq \mathcal{N}^+$  where

$$\begin{aligned}
 \mathcal{N}^- & \stackrel{\text{def}}{=} \cup_{i=1}^m \mathcal{N}_i^-; \quad \text{where } \mathcal{N}_i^- \stackrel{\text{def}}{=} \{(\delta_1, \dots, \delta_m) | \delta_i \in \mathcal{N}_0; \delta_{t \neq i} = \mathbf{0}\}. \\
 \mathcal{N}^+ & \stackrel{\text{def}}{=} \{(\alpha_1 \delta_1, \dots, \alpha_m \delta_m) | \sum_{i=1}^n \alpha_i = 1; \alpha_i \geq 0, \delta_i \in \mathcal{N}_0, i = 1, \dots, m\}.
 \end{aligned}$$

$\mathcal{N}_i^-$  contains  $m$  perturbations where only one pair of features are targeted for manipulation from  $\mathcal{N}_0$  and others are zero vectors.

$\mathcal{N}^- \subseteq \mathcal{N} \subseteq \mathcal{N}^+$  naturally indicates that

$$\begin{aligned}
 & \min_{(\delta_1, \dots, \delta_m) \in \mathcal{N}^+} \sum_{i=1}^m l_i \mathcal{I}_i(\mathbf{x} + \delta_i) \\
 & \leq \min_{(\delta_1, \dots, \delta_m) \in \mathcal{N}} \sum_{i=1}^m l_i \mathcal{I}_i(\mathbf{x} + \delta_i) \\
 & \leq \min_{(\delta_1, \dots, \delta_m) \in \mathcal{N}^-} \sum_{i=1}^m l_i \mathcal{I}_i(\mathbf{x} + \delta_i).
 \end{aligned} \tag{21}$$

We approximate  $\mathcal{I}_i(\mathbf{x} + \delta_i)$  by Taylor expansion  $\mathcal{I}_i(\mathbf{x} + \delta_i) = \mathcal{I}_i(\mathbf{x}) + H_i(\mathbf{x})^\top \delta_i$ , where  $H_i(\mathbf{x})$  is the  $i$ -th row of Hessian matrix. We aim to prove that

$$\min_{(\delta_1, \dots, \delta_m) \in \mathcal{N}} \sum_{i=1}^m l_i \mathcal{I}_i(\mathbf{x} + \delta_i) \tag{22}$$

is equivalent to

$$\nu = \sum_{i=1}^n l_i \mathcal{I}_i(\mathbf{x}) - \epsilon \max_t \|H_t(\mathbf{x})\|_2 \tag{23}$$

since  $\nu$  is not smaller than the rightmost term and not larger than the leftmost term in Eq. (21).

**To prove**  $\nu \geq \min_{(\delta_1, \dots, \delta_m) \in \mathcal{N}^-} \sum_{i=1}^m l_i \mathcal{I}_i(\mathbf{x} + \delta_i)$ .

$$\begin{aligned}
 & \min_{(\delta_1, \dots, \delta_m) \in \mathcal{N}^-} \sum_{i=1}^m l_i \mathcal{I}_i(\mathbf{x} + \delta_i) \\
 & \leq \min_{(\delta_1, \dots, \delta_m) \in \mathcal{N}_i^-} \sum_{i=1}^m l_i \mathcal{I}_i(\mathbf{x} + \delta_i) \\
 & = \min_{(\delta_1, \dots, \delta_m) \in \mathcal{N}_i^-} \sum_{i=1}^m l_i \mathcal{I}_i(\mathbf{x}) + l_i H_i(\mathbf{x})^\top \delta_i \\
 & = \sum_{i=1}^m l_i \mathcal{I}_i(\mathbf{x}) + \sum_{i=1}^m \min_{(\delta_1, \dots, \delta_m) \in \mathcal{N}_i^-} l_i H_i(\mathbf{x})^\top \delta_i \\
 & = \sum_{i=1}^m l_i \mathcal{I}_i(\mathbf{x}) + \min_{t \in \{1, \dots, m\}} \min_{\delta_t \in \mathcal{N}_0} l_t H_t(\mathbf{x})^\top \delta_t \\
 & = \sum_{i=1}^m l_i \mathcal{I}_i(\mathbf{x}) - \epsilon \max_{t \in \{1, \dots, m\}} \|H_t(\mathbf{x})\|_2.
 \end{aligned}$$

The inequality on line-2 holds since  $\mathcal{N}_i^- \subseteq \mathcal{N}^-$ . The equality on line-5 holds due to the definition of  $\mathcal{N}_i^-$ , where only one  $\delta_t$  of  $(\delta_1, \dots, \delta_m)$  is from  $\mathcal{N}_0$  and the rest are all zeros. The equality on line-6 holds by picking  $\delta_t = -l_t H_t(\mathbf{x})$ .

**To prove**  $\nu \leq \min_{(\delta_1, \dots, \delta_m) \in \mathcal{N}^+} \sum_{i=1}^m l_i \mathcal{I}_i(\mathbf{x} + \delta_i)$ .

$$\begin{aligned}
 & \min_{(\delta_1, \dots, \delta_m) \in \mathcal{N}^+} \sum_{i=1}^m l_i \mathcal{I}_i(\mathbf{x} + \delta_i) \\
 & = \min_{\sum_i \alpha_i = 1, \alpha_i \geq 0, \delta_i \in \mathcal{N}_0} \sum_{i=1}^m l_i \alpha_i \mathcal{I}_i(\mathbf{x} + \hat{\delta}_i) \\
 & = \sum_{i=1}^m l_i \mathcal{I}_i(\mathbf{x}) + \min_{\sum_i \alpha_i = 1, \alpha_i \geq 0} \sum_{i=1}^m \alpha_i \min_{\delta_i \in \mathcal{N}_0} l_i H_i(\mathbf{x})^\top \delta_i \\
 & = \sum_{i=1}^m l_i \mathcal{I}_i(\mathbf{x}) + \min_{t \in \{1, \dots, m\}} \min_{\delta_t \in \mathcal{N}_0} l_t H_t(\mathbf{x})^\top \delta_t \\
 & = \sum_{i=1}^m l_i \mathcal{I}_i(\mathbf{x}) - \epsilon \max_{t \in \{1, \dots, m\}} \|H_t(\mathbf{x})\|_2.
 \end{aligned}$$

**Connection between AT and R2ET.** By comparing  $\min_{(\delta_1, \dots, \delta_m) \in \mathcal{N}^-} \sum_{i=1}^m l_i \mathcal{I}_i(\mathbf{x} + \delta_i) \leq \nu = \min_{(\delta_1, \dots, \delta_m) \in \mathcal{N}^+} \sum_{i=1}^m l_i \mathcal{I}_i(\mathbf{x} + \delta_i)$  with Eq. (21), we could establish the equivalence between Eq. (22) and Eq. (23). We further add  $\mathcal{L}_{cls}$  and taking the maximization over  $\mathbf{w}$  on both terms, which indicates that the goal of AT in Eq. (20) is equivalent to

$$\max_{\mathbf{w}} -\mathcal{L}_{cls} + \sum_{i=1}^m l_i \mathcal{I}_i(\mathbf{x}) - \epsilon \max_t \|H_t(\mathbf{x})\|_2, \quad (24)$$

or

$$\min_{\mathbf{w}} \mathcal{L}_{cls} - \sum_{i=1}^m l_i \mathcal{I}_i(\mathbf{x}) + \epsilon \max_t \|H_t(\mathbf{x})\|_2. \quad (25)$$

Notice that  $\min_{\mathbf{w}} \max_t \|H_t(\mathbf{x})\|_2 \rightarrow 0$  if and only if  $\min_{\mathbf{w}} \|H(\mathbf{x})\|_2 \rightarrow 0$ . Further replacing  $\min_{\mathbf{w}} \max_t \|H_t(\mathbf{x})\|_2$  by  $\min_{\mathbf{w}} \|H(\mathbf{x})\|_2$  indicates the equivalent between Eq. (20) and

$$\min_{\mathbf{w}} \mathcal{L}_{cls} - \sum_{i=1}^m l_i \mathcal{I}_i(\mathbf{x}) + \epsilon \|H(\mathbf{x})\|_2. \quad (26)$$

The equivalence between Eq. (6) and Eq. (17) can be proved similarly by considering all inputs  $\mathbf{x}$  in the training set.

### A.3. A multi-objective attacking algorithm and its analysis

We present an algorithm that will terminate in finite iterations, and flip the first pair of salient and non-salient features, or claim a failed attack. The algorithm is based on a trust-region method designed for single non-convex but smooth objective with nonlinear and non-convex equality constraints (Cartis et al., 2014).

Let the output vector  $f(\mathbf{x}) = [f_1(\mathbf{x}), \dots, f_C(\mathbf{x})]$ . Given  $n$  features and top- $k$  salient features, there are  $m = k \times (n - k)$  objectives that can be indexed by subscripts  $\ell$  so that the objective vector becomes  $[h_1(\mathbf{x}), \dots, h_\ell(\mathbf{x}), \dots, h_m(\mathbf{x})]$ . Let  $\|\cdot\|$  be a convex norm with Lipschitz constant 1.

Since we are working with numerical algorithms, an approximately feasible set will be appropriate. Define the following constrained MOO problem

$$\begin{aligned}
 & \min_{\mathbf{x}} [h_1(\mathbf{x}), \dots, h_\ell(\mathbf{x}), \dots, h_m(\mathbf{x})], \quad (27) \\
 & \text{s.t. } \|f(\mathbf{x}) - f(\mathbf{x}^{(0)})\| \leq \epsilon_f, \\
 & \quad \|\mathbf{x} - \mathbf{x}^{(0)}\|_2 \leq \epsilon_x
 \end{aligned}$$

In the following analysis, we ignore the constraint  $\|\mathbf{x} - \mathbf{x}^{(0)}\|_2 \leq \epsilon_x$ , since it can be combined with the first constraint to obtain a new constraint

$$\|\tilde{f}(\mathbf{x}) - \tilde{f}(\mathbf{x}_0)\| \leq \epsilon, \quad (28)$$

for some  $\epsilon > 0$ , with

$$\tilde{f}(\mathbf{x}) = [f(\mathbf{x}), \mathbf{x}]. \quad (29)$$

Therefore, we let  $f$  denote  $\tilde{f}$  to simplify the notation. Define the domain

$$\mathcal{C}_1 \stackrel{\text{def}}{=} \{\mathbf{x} : \|f(\mathbf{x}) - f(\mathbf{x}^{(0)})\| \leq \epsilon\}. \quad (30)$$

**Assumption H.1:** The constraint function  $f(\mathbf{x})$  is continuously differentiable on the domain  $\mathbb{R}^n$ , and the objective functions  $h_\ell$ ,  $\ell = 1, \dots, m$ , are continuously differentiable in the set

$$\mathcal{C}_2 \stackrel{\text{def}}{=} \mathcal{C}_1 + \mathcal{B}(0, \delta \Delta^{(1)}), \quad (31)$$

where  $\delta > 1$  is a constant,  $\Delta^{(1)}$  is the initial radius argument for the trust-region method for multi-objective optimization TR-MOO( $\mathbf{x}, \Delta$ ) to be defined below, and  $\mathcal{B}(0, \delta\Delta^{(1)})$  is an open ball centered at 0 of radius  $\delta\Delta^{(1)}$ .

**Assumption H.2:** The constraint function  $f(\mathbf{x})$ 's is continuously differentiable on the domain  $\mathbb{R}^n$ , and the objective functions  $h_\ell$ ,  $\ell = 1, \dots, m$ , are continuously differentiable in the set

$$\mathcal{C}_2 \stackrel{\text{def}}{=} \mathcal{C}_1 + \mathcal{B}(0, \delta\Delta^{(1)}), \quad (32)$$

where  $\delta > 1$  is a constant,  $\Delta^{(1)}$  is the initial radius argument for the trust-region method for multi-objective optimization TR-MOO( $\mathbf{x}, \Delta$ ) to be defined below, and  $\mathcal{B}(0, \delta\Delta^{(1)})$  is an open ball centered at 0 of radius  $\delta\Delta^{(1)}$ .

**Assumption H.3:** The objective functions  $h_\ell$ ,  $\ell = 1, \dots, m$  are bounded below and above in the set  $\mathcal{C}_1$ . More specifically,

$$h_{\text{low}} \stackrel{\text{def}}{=} \min_{\ell} \{ \min_{\mathbf{x}} h_1(\mathbf{x}), \dots, \min_{\mathbf{x}} h_m(\mathbf{x}) \}, \quad (33)$$

$$h_{\text{up}} \stackrel{\text{def}}{=} \max_{\ell} \{ \max_{\mathbf{x}} h_1(\mathbf{x}), \dots, \max_{\mathbf{x}} h_m(\mathbf{x}) \}. \quad (34)$$

We give an attacking algorithm MOO-attack below that can either find the first feature pair to flip in an explanation, or to claim that it is impossible to flip any feature pair. In the algorithm, superscript  $(k)$ ,  $k = 1, 2, \dots$  indicates the number of iterations.

$$\text{TR-MOO}(\mathbf{x}, \Delta) \quad \begin{cases} \min_{\alpha, \mathbf{d}} & \alpha \\ \text{s.t.} & l_{\phi_\ell}(\mathbf{x}, t, \mathbf{d}) \leq \alpha, \ell = 1, \dots, m, \\ & \|\mathbf{d}\| \leq \Delta. \end{cases}$$

The attacking algorithm may not be able to flip any pair of features when  $\min_{1 \leq \ell \leq m} \chi_\ell(\mathbf{x}^{(k)}, t^{(k)}) < \epsilon$ , but there can be other objective functions that still have  $\chi_\ell(\mathbf{x}^{(k)}, t^{(k)}) \geq \epsilon$  and there is a chance to flip the corresponding pairs of features. We will remove any objective function  $h_\ell$  with  $\chi_\ell(\mathbf{x}^{(k)}, t^{(k)}) < \epsilon$  and return to the while loop to try to flip other pairs of features. If all objective functions are removed at the end, the attacker fails to attack the explanation.

We adapt the theoretical results from (Cartis et al., 2014) to the above multi-objective optimization algorithm to show a global convergence rate for the attacker.

First, the following lemma shows sufficient descent in the linearized merit functions in the direction  $\mathbf{d}^{(k)}$ .

**Lemma A.4.** Suppose that assumption A.1 holds. If  $\mathbf{x}^{(k)} \in \mathcal{C}_1$  defined in Eq. (30), then

$$\begin{aligned} l_{\phi_\ell}(\mathbf{x}^{(k)}, t_\ell^{(k)}, 0) - l_{\phi_\ell}(\mathbf{x}^{(k)}, t_\ell^{(k)}, \mathbf{d}^{(k)}) \\ \geq \min(\Delta^{(k)}, 1) \chi_\ell(\mathbf{x}^{(k)}, t^{(k)}), \end{aligned} \quad (35)$$

for each linearized merit function  $l_{\phi_\ell}$  defined in Eq. (10).

---

**Algorithm 1** Attacking a pair of features
 

---

**Input:** initial input  $\mathbf{x}$ , target model  $f$ , current explanation  $\mathcal{I}(\mathbf{x})$ , tolerance  $\epsilon > 0$ , trust-region method parameters  $1 > \eta > 0$  and  $1 > \gamma > 0$ .

Set  $k = 1$ ,  $\mathbf{x}^{(k)} = \mathbf{x}$ ,  $t_\ell^{(k)} = \|f(\mathbf{x}^{(k)})\| + h_\ell(\mathbf{x}^{(k)}) - \epsilon^{(k)}$  for each objective  $h_\ell$ .

**while**  $\min_{1 \leq \ell \leq m} \chi_\ell(\mathbf{x}^{(k)}, t^{(k)}) \geq \epsilon$  **do**

Solve TR-MOO( $\mathbf{x}^{(k)}, \Delta^{(k)}$ ) to obtain a joint descent direction  $\mathbf{d}^{(k)}$  for all linearized merit functions  $l_{\phi_\ell}$ .

$\rho_\ell^{(k)} = \frac{\phi_\ell(\mathbf{x}^{(k)}, t_\ell^{(k)}) - \phi_\ell(\mathbf{x}^{(k)} + \mathbf{d}^{(k)}, t_\ell^{(k)})}{l_{\phi_\ell}(\mathbf{x}^{(k)}, t_\ell^{(k)}, 0) - l_{\phi_\ell}(\mathbf{x}^{(k)}, t_\ell^{(k)}, \mathbf{d}^{(k)})}$  for each  $\ell = 1, \dots, m$ .

**if**  $\min_\ell \rho_\ell^{(k)} > \eta$  **then**

$\mathbf{x}^{(k+1)} = \mathbf{x}^{(k)} + \mathbf{d}^{(k)}$ .

$\Delta^{(k+1)} = \Delta^{(k)}$ .

**if**  $h_\ell(\mathbf{x}^{(k)}) \geq t_\ell^{(k)}$  **then**

$t_\ell^{(k+1)} = t_\ell^{(k)} - \phi_\ell(\mathbf{x}^{(k)}, t_\ell^{(k)}) + \phi_\ell(\mathbf{x}^{(k+1)}, t_\ell^{(k)})$ .

**else**

$t_\ell^{(k+1)} = 2h_\ell(\mathbf{x}^{(k+1)}) - t_\ell^{(k)} - \phi_\ell(\mathbf{x}^{(k)}, t_\ell^{(k)}) + \phi_\ell(\mathbf{x}^{(k+1)}, t_\ell^{(k)})$ .

**end if**

**end if**

$\mathbf{x}^{(k+1)} = \mathbf{x}^{(k)}$ .

$\Delta^{(k+1)} = \gamma\Delta^{(k)}$ .

$t_\ell^{(k+1)} = t_\ell^{(k)}$  for  $\ell = 1, \dots, m$ .

**end if**

**end while**

---

The proof can be found in Lemma 2.1 in (Cartis et al., 2014).

The next lemma shows that from iteration to iteration during the while loop in Algorithm 1, the following invariant will be maintained.

**Lemma A.5.** *Suppose that assumption A.1 holds. In each iteration for  $k \geq 1$  in Algorithm 1, the following properties hold:*

$$h_\ell(\mathbf{x}^{(k)}) - t_\ell^{(k)} > 0, \ell = 1, \dots, m, \quad (36)$$

$$\phi_\ell(\mathbf{x}^{(k)}, t_\ell^{(k)}) = \epsilon, \ell = 1, \dots, m, \quad (37)$$

$$|h_\ell(\mathbf{x}^{(k)}) - t_\ell^{(k)}| \leq \epsilon, \ell = 1, \dots, m, \quad (38)$$

$$\|f(\mathbf{x}^{(k)})\| \leq \epsilon. \quad (39)$$

The proof can be obtained via applying Lemma 2.2 in (Cartis et al., 2014) to each of the objective functions independently.

The last inequality indicates that during the attack, the manipulated input  $\mathbf{x}^{(k)}$  remains in the approximate feasible set  $\mathcal{C}_1$  and that the prediction by  $f$  is not changed. This is important to make the attack stealthy. The second last inequality shows that each objective  $h_\ell$  will chase the corresponding target  $t_\ell^{(k)}$  over the iterations, so that if  $t_\ell^{(k)}$  can be shown to be decreasing sufficiently fast, we can show the convergence of  $h_\ell$ . Note that different targets  $t_\ell^{(k)}$  will move in different speed, as they are updated independently in the algorithm. Also, a target is not guarantee to be reduced below zero for  $h_\ell$  to become negative and the  $\ell$ -th pair of features will be flipped.

The next lemma shows that when the radius  $\Delta^{(k)}$  used in TR-MOO( $\mathbf{x}^{(k)}$ ,  $\Delta^{(k)}$ ) is small enough, the radius won't be further reduced. Together with Lemma A.4, the linearized merit functions are reduced sufficiently per iteration.

**Lemma A.6.** *Suppose that assumptions A.1 and A.2 hold. Then with  $\min_\ell \chi_\ell(\mathbf{x}^{(k)}, t^{(k)}) \geq \epsilon$  and*

$$\Delta^{(k)} \leq \min_\ell \frac{(1-\eta)\epsilon}{L_{g_\ell} + \frac{1}{2}L_J}, \quad (40)$$

*we will have the condition  $\min_\ell \rho_\ell^{(k)} > \eta$  in Algorithm 1 hold true and  $\Delta^{(k+1)} = \Delta^{(k)}$ . Further more, with  $\min_\ell \chi_\ell(\mathbf{x}^{(k)}, t^{(k)}) \geq \epsilon$ , we have, for all  $k \geq 1$ ,*

$$\Delta^{(k)} \geq \min \left( \Delta^{(1)}, \min_\ell \frac{(1-\eta)\gamma}{L_{g_\ell} + \frac{1}{2}L_J} \right) \epsilon. \quad (41)$$

The proof is a modification to the proof of Lemma 3.2 in (Cartis et al., 2014), with the derivation done for each of the objective function  $h_\ell$  to guarantee sufficient descent in all merit functions. An interesting observation is that the search radius  $\Delta^{(k)}$  is restricted by the objective that has the most rapid change in its gradient  $g_\ell$  (characterized by  $L_{g_\ell}$ ). If all objectives are smooth (with small  $L_{g_\ell}$ ), the search

radius can be larger and reduction in the merit functions is larger. The second inequality of the above lemma says that the search radius will have a lower bound across all iterations.

How many times do we need to reduce the search radius is characterized in the following lemma.

**Lemma A.7.** *There are at most  $O(\lceil \log(\epsilon) \rceil)$  number of times that  $\Delta^{(k)}$  will be reduced by the factor of  $\gamma$ .*

That is because, starting from  $\Delta^{(1)}$ , once  $\Delta^{(k)}$  falls below  $\min_\ell \frac{(1-\eta)\epsilon}{L_{g_\ell} + \frac{1}{2}L_J}$  at iteration  $k$ , there will be no more reduction in future iterations.

The following lemma show sufficient reduction in the merit functions and the targets.

**Lemma A.8.** *Suppose that assumptions A.1 and A.2 hold. Whenever  $\mathbf{x}^{(k)}$  is updated in Algorithm 1, for each objective function  $h_\ell$ , both the reductions  $\phi_\ell(\mathbf{x}^{(k)}, t_\ell^{(k)}, 0) - \phi_\ell(\mathbf{x}^{(k)}, t_\ell^{(k)}, \mathbf{d}^{(k)})$  and  $t_\ell^{(k)} - t_\ell^{(k)}$  are at least*

$$\min \left( \Delta^{(1)}, \min_\ell \frac{(1-\eta)\gamma}{L_{g_\ell} + \frac{1}{2}L_J} \right) \epsilon^2 \eta. \quad (42)$$

The proof is to use the condition that  $\rho_\ell^{(k)} > \eta$  for all  $\ell = 1, \dots, m$ , Eq. (35), the condition that  $\min_{1 \leq \ell \leq m} \chi_\ell(\mathbf{x}^{(k)}, t^{(k)}) \geq \epsilon$ , and Eq. (41).

Lastly, we present the main global convergence results. Let  $h_{\text{low}} \stackrel{\text{def}}{=} \min_\ell \{ \min_{\mathbf{x}} h_1(\mathbf{x}), \dots, \min_{\mathbf{x}} h_m(\mathbf{x}) \}$  and  $h_{\text{up}} \stackrel{\text{def}}{=} \max_\ell \{ \max_{\mathbf{x}} h_1(\mathbf{x}), \dots, \max_{\mathbf{x}} h_m(\mathbf{x}) \}$ .

**Theorem A.9.** *Suppose assumptions A.1-A.3 hold. Then Algorithm 1 generates an  $\epsilon$ -first-order critical point for problem Eq. (27) in at most*

$$\left\lceil \frac{(h_{\text{up}} - h_{\text{low}}) \frac{\kappa}{\epsilon^2}}{\epsilon^2} \right\rceil \quad (43)$$

*iterations of the while loop in the algorithm, where  $\kappa$  is a constant independent of  $\epsilon$  but depending on  $\gamma, \eta, L_{h_\ell}$ , and  $L_J$ .*

The proof hinge on the following inequality

$$h_{\text{low}} \leq h_\ell(\mathbf{x}^{(k)}) \quad (44)$$

$$\leq t_\ell^{(k)} + \epsilon \quad (45)$$

$$\leq t_\ell^{(1)} - i_k \kappa_2 \epsilon^2 + \epsilon \quad (46)$$

$$\leq h_\ell(\mathbf{x}^{(1)}) - i_k \kappa_2 \epsilon^2 + \epsilon \quad (47)$$

$$\leq h_{\text{up}} - i_k \kappa_2 \epsilon^2 + \epsilon \quad (48)$$

where  $i_k$  is the number of iterations between 1 and  $k$  where  $\min_\ell \rho_\ell^{(k')} > \eta, 1 \leq k \leq k'$ , is true.

$$\kappa_2 = \min \left( \Delta^{(1)}, \min_\ell \frac{(1-\eta)\gamma}{L_{g_\ell} + \frac{1}{2}L_J} \right) \eta. \quad (49)$$

Therefore,

$$i_k \leq \left\lceil \frac{h_{\text{up}} - h_{\text{low}} + \epsilon}{\kappa_2 \epsilon^2} \right\rceil. \quad (50)$$

Since  $O(\lceil \log(\epsilon) \rceil)$  grows slower than  $1/\epsilon^2$ , the overall number of iterations is in the order of  $\left\lceil (h_{\text{up}} - h_{\text{low}}) \frac{\kappa}{\epsilon^2} \right\rceil$ .

*Comments:*

- If after the while loop, no  $h_\ell$  is reduced to a negative value, then one remove those  $h_\ell$  that has reached the approximate critical point and continue the while loop with the remaining objective functions. The next while loop starts with a smaller gap  $h_{\text{up}} - h_{\text{low}}$  defined over the remaining objectives. Since there are a finite number of objectives, the algorithm finishes in finite iterations.
- The constraint  $\|f(\mathbf{x}) - f(\mathbf{x}^{(0)})\| \leq \epsilon$  is maintained over all iterations and thus stay stealthy during the attack.

#### A.4. Statistical robustness

We will use tools for generalization error analysis on any single input  $\mathbf{x}$  (a vector, an image, or a graph) to prove that with a high probability, the empirical error of ranking salient features of  $\mathbf{x}$  for a fixed model  $f$  is not too far away from the true error of ranking the same set of salient features, with respect to random sampling of  $\mathbf{x}$  from an arbitrary distribution  $\mathcal{D}$  on a support set around  $\mathbf{x}$  where the salient features are preserved.  $\mathcal{D}$  depends on  $\mathbf{x}$ .

**Roadmap:** We first adopt the McDairmid’s inequality for *dependent* variables to show a concentration inequality for ranking errors of a fixed feature ranking function based on the salient score function  $\mathcal{I}(\mathbf{x})$ . Then we will adopt the standard covering number argument as in (Agarwal, 2011; Rudin, 2009) to prove uniform convergence that depends on the margin in the empirical ranking loss, therefore justifying the maximization of the gap/thickness between the scores of salient and non-salient features in R2ET.

**Basic definitions.** Given  $\mathcal{I}$  and  $\mathbf{x}$ , define the true and empirical 0-1 risks

$$R_{0,1}^{\text{true}}(\mathcal{I}, \mathbf{x}) = \mathbb{E}_{\mathbf{x}' \sim \mathcal{D}} \left[ \frac{1}{m} \sum_{i=1}^k \sum_{j=1}^n \mathbb{1}[\mathcal{I}_i(\mathbf{x}') < \mathcal{I}_j(\mathbf{x}')] \right], \quad (51)$$

$$R_{0,1}^{\text{emp}}(\mathcal{I}, \mathbf{x}) = \frac{1}{m} \sum_{i=1}^k \sum_{j=1}^n \mathbb{1}[\mathcal{I}_i(\mathbf{x}) < \mathcal{I}_j(\mathbf{x})]. \quad (52)$$

To relate the risks to the thickness, we the loss  $\phi_u(z)$ ,  $u > 0$ , that is similar to the hinge loss

$$\phi_u(z) = \begin{cases} 1 & z < 0, \\ 1 - z/u & 0 \leq z < u, \\ 0 & z \geq u. \end{cases} \quad (53)$$

Based on  $\phi_u$ , we define the surrogate true and empirical risks

$$R_{\phi,u}^{\text{true}}(\mathcal{I}, \mathbf{x}) = \mathbb{E}_{\mathbf{x}' \sim \mathcal{D}} \left[ \frac{1}{m} \sum_{i=1}^k \sum_{j=1}^n \phi_u(\mathcal{I}_i(\mathbf{x}') - \mathcal{I}_j(\mathbf{x}')) \right], \quad (54)$$

$$R_{\phi,u}^{\text{emp}}(\mathcal{I}, \mathbf{x}) = \frac{1}{m} \sum_{i=1}^k \sum_{j=1}^n \phi_u(\mathcal{I}_i(\mathbf{x}) - \mathcal{I}_j(\mathbf{x})). \quad (55)$$

The boundedness and the Lipschitzness of  $\phi_u$  will be useful for proving the follow lemma and theorem.

Lastly, an upper bound of  $\phi_u(z)$  can be defined as a large-margin 0-1 loss: if  $z \geq u$ , the loss is 0, and otherwise, the loss is 1. The corresponding empirical risk

$$R_{0,1,u}^{\text{emp}}(\mathcal{I}, \mathbf{x}) = \frac{1}{m} \sum_{i=1}^k \sum_{j=1}^n \mathbb{1}[\mathcal{I}_i(\mathbf{x}) < \mathcal{I}_j(\mathbf{x}) + u]. \quad (56)$$

counts how many pairs of salient and non-salient features that are the salient feature is  $u$  less salient than the non-salient feature according to  $\mathcal{I}$ .

**Generalization bound of  $R_{\phi,u}^{\text{emp}}(\mathcal{I}, \mathbf{x})$  for a specific  $\mathcal{I}$ .** As we randomly sample  $\mathbf{x}'$  from  $\mathcal{D}$ , the terms  $\mathcal{I}_i(\mathbf{x}')$  and the associated 0-1 and  $\phi_u$  losses The typical McDiarmid’s inequality bounds the probability of a function of multiple independent random variables from the expectation of the function. The elements in  $R_{\phi,u}^{\text{emp}}$  are not independent. The saliency scores of different features are dependent since they are function of the same model  $f$ , the input  $\mathbf{x}$ , and the mechanism that calculate the gradients for  $\mathcal{I}$ . In (Usunier et al., 2005), the authors generalized the inequality to dependent variables, and we adopt their conclusion as follows:

**Lemma A.10.** *Given prediction model  $f$ , saliency map  $\mathcal{I}$ , input  $\mathbf{x}$ , distribution  $\mathcal{D}$  surrounding  $\mathbf{x}$ , surrogate loss  $\phi_u$ , and a constant  $\epsilon > 0$ , we have*

$$\Pr_{\mathbf{x}' \sim \mathcal{D}} \left\{ R_{\phi,u}^{\text{true}}(\mathcal{I}, \mathbf{x}') \geq R_{\phi,u}^{\text{emp}}(\mathcal{I}, \mathbf{x}) + \epsilon \right\} \leq 2 \exp \left( -\frac{2m\epsilon^2}{\chi} \right), \quad (57)$$

where  $\chi$  is the chromatic number of the dependency graph of the pairs of random variables  $(\mathcal{I}_i, \mathcal{I}_j)$  for any  $1 \leq i \leq k$  and  $k+1 \leq j \leq n$ .

*Comments:*

- The above dependency graph describes when two pairs of random variables  $(\mathcal{I}_i, \mathcal{I}_j)$  (regarded as a random vector) and  $(\mathcal{I}_{i'}, \mathcal{I}_{j'})$  (regarded as another random vector) are dependent. In particular, the two nodes  $(\mathcal{I}_i, \mathcal{I}_j)$  and  $(\mathcal{I}_{i'}, \mathcal{I}_{j'})$  are linked if they are dependent. This graph depends on  $\mathcal{I}$ ,  $\mathbf{x}$ , and  $\mathcal{D}$  and is in general unknown.

- The chromatic number of the dependency graph is upper-bounded by 1 plus the maximum degree of nodes on the dependency graph, which is  $1+m$ . In the worst case, the bounds in Eq. (57) approximates  $2\exp(-2\epsilon^2)$  as  $m$  becomes sufficiently large.

**Uniform convergence of the class of saliency score functions.** Since R2ET searches the optimal  $\mathcal{I}$  function from a class  $\mathcal{F}$  of such functions given  $f, \mathcal{I}, \mathbf{x}$ , and  $\mathcal{D}$ ,  $u > 0$ , with the preference over  $\mathcal{I}$  that has a large gap  $u$  so that  $\mathcal{I}_i(\mathbf{x}) > \mathcal{I}_j(\mathbf{x}) + u$  for salient feature  $i$  and non-salient feature  $j$ .

**Theorem A.11.** *Given prediction model  $f$ , input  $\mathbf{x}$ , surrogate loss  $\phi_u$ , and a constant  $\epsilon > 0$ , for arbitrary saliency map  $\mathcal{I} \in \mathcal{F}$  and any distribution  $\mathcal{D}$  surrounding  $\mathbf{x}$  that preserves the salient features in  $\mathbf{x}$ , we have*

$$\Pr_{\mathbf{x}' \sim \mathcal{D}} \{R_{0,1}^{\text{true}}(\mathcal{I}, \mathbf{x}') \geq R_{0,1,u}^{\text{emp}}(\mathcal{I}, \mathbf{x}) + \epsilon\} \leq 2\mathcal{N}(\mathcal{F}, \frac{\epsilon u}{8}) \exp\left(-\frac{2m\epsilon^2}{\chi}\right), \quad (58)$$

where  $\mathcal{N}(\mathcal{F}, \frac{\epsilon u}{8})$  is the covering number of the functional space  $\mathcal{F}$  with radius  $\frac{\epsilon u}{8}$  (Zhang, 2002).

Comments:

- The proof is standard and a similar proof can be found in (Rudin, 2009).
- With a larger  $u > 0$ , the empirical risk  $R_{0,1,u}^{\text{emp}}(\mathcal{I}, \mathbf{x})$  will increase as more pairs of salient and non-salient features will not have their saliency score larger than this gap. On the other hand, the covering number  $\mathcal{N}(\mathcal{F}, \frac{\epsilon u}{8})$  will decrease as  $u$  increases as a larger radius can cover more  $\mathcal{I} \in \mathcal{F}$ . This represents a model selection problem.
- Last but not least important, with a larger gap  $u$  that R2ET can optimize  $\mathcal{I}$ , with a random perturbation of  $\mathbf{x}$  to  $\mathbf{x}'$  that has the same saliency features, the true risk (representing how bad the true explanations can be perturbed) will be low.

## B. Details of Experiments

This section provides more details about the experimental settings and additional results, as supplementary for Sec. 5.

### B.1. Training with R2ET

Algorithm 2 provides a way to train the model with R2ET.

### B.2. Datasets

Our experiments use two types of network architectures: single-input DNNs and dual-input SNs. For single-input DNNs, we use three tabular datasets, Adult, Bank (Moro et al., 2014) and COMPAS (Mothilal et al., 2020). We divide

**Algorithm 2** Training a model with robust ranking explanation by R2ET.

**Input:** Training set  $(\mathcal{X}_T, \mathcal{Y}_T)$  and validation set  $(\mathcal{X}_V, \mathcal{Y}_V)$ ;  $k$  as number of features of interest; hyperparameter  $\lambda_1 > 0, \lambda_2 > 0$ .

```

1: if exists a pretrain model  $f_{pre}$  then
2:    $f(\mathbf{w}) \leftarrow f_{pre}$ 
3: end if
4: for  $iteration \leq MaxIter$  do
5:   calculate  $\mathcal{L}_{total}$  of R2ET by Eq. (6)
6:    $\mathbf{w} \leftarrow \mathbf{w} - \eta \nabla \mathcal{L}_{total}$ 
7:   if eval( $f, \mathcal{X}_V, \mathcal{Y}_V$ ) gets better then
8:     save model  $f(\mathbf{w})$  to file
9:   end if
10: end for
11: load and output model  $f(\mathbf{w})$  from file
    
```

each tabular dataset into training, validation and test portions at a ratio of 70 : 15 : 15, respectively. The original tabular datasets contain a mixture of strings and floating numbers. Thus, we binarize them and map them to 28-dim, 18-dim, and 16-dim feature spaces, respectively (Chen et al., 2021). We also conduct experiments on CIFAR-10 (Krizhevsky et al., 2009) with ResNet (He et al., 2016), where the training set is further divided into the training and validation portion with a ratio of 80 : 20. For dual-input SNs, we use one image dataset, MNIST (LeCun et al., 1998), and two graph datasets, BP (Ma et al., 2019) and ADHD. For MNIST, we randomly select 2400 pairs of images with digits 3 and 8 from training images as the training set, and 300 and 600 pairs from test images as the validation and test sets, respectively. In BP and ADHD, each brain network comprises 82 and 116 nodes, respectively. Since the datasets are limited, we employ five-fold cross-validation, where three folds are used for training, one for validation, and one for testing. We create training sets by pairing any two training graphs. We pair any two training graphs as the training set. To simulate real medical diagnosis (by comparing a new sample with those in the database), each pair consists of a training graph and a validation (or test) graph as validation (or testing) sets.

### B.3. Evaluation Metrics

For the target sample  $\mathbf{x}$  and the corresponding adversarial sample  $\mathbf{x}' = \mathbf{x} + \delta$ , we evaluate the robustness of ranking explanations by measuring the similarity between explanations,  $\mathcal{I}(\mathbf{x}) \in \mathbb{R}^n$  and  $\mathcal{I}(\mathbf{x}') \in \mathbb{R}^n$ . We use Precision@ $k$ , (P@ $k$ ) to quantify the *similarity*.

- **Precision@ $k$  (P@ $k$ ).** It is widely used to evaluate the robustness of explanations (Ghorbani et al., 2019; Wang

et al., 2020c). Formally,

$$P@k(\mathcal{I}(\mathbf{x}), \mathcal{I}(\mathbf{x}')) = \frac{|\mathcal{I}(\mathbf{x})_{[k]} \cap \mathcal{I}(\mathbf{x}')_{[k]}|}{k},$$

where  $\mathcal{I}(\mathbf{x})_{[k]}$  is the set of the  $k$  most important features of the explanation  $\mathcal{I}(\mathbf{x})$ .  $|\cdot|$  counts the number of elements in the intersection of two top  $k$  features.

Besides robustness, we use the following metrics to evaluate the model’s *classification performance*. Related discussion and results can be found in Appendix B.6.4 and B.6.5.

- **Clean AUC (cAUC) and adversarial AUC (aAUC).** An explanation-robust model should also have robust classification performance, so we use the metric cAUC and aAUC to measure the model’s classification performance before and after the attack, respectively.
- **Sensitivity (Sen).** Since adversarial attacks can be detected by checking the consistency of predictions (Xu et al., 2020), we use Sen to measure the ratio at which the predicted classification of the perturbed sample changes. More specifically, Sen measures the ratio at which classification result changes after an attack for single-input DNNs. For dual-input SNs, there are three classification results for a pair of samples: one similarity classification result and two classification results from the classifier with respect to two samples, respectively. Thus, Sen for SNs measures the ratio at which *any* of three classification results change after attacks.

We consider three widely adopted metrics to evaluate the *faithfulness* of explanations. The numerical results can be found in Table 7.

- **Decision Flip - Fraction of Tokens (DFFOT) (Serrano & Smith, 2019)** measures the minimum fraction of important features to be removed to flip the prediction. A *lower* DFFOT indicates a more faithful explanation. Formally,

$$\text{DFFOT} = \min_k \frac{k}{n}, \quad \text{s.t. } \arg \max_c f_c(\mathbf{x}) \neq \arg \max_c f_c(\mathbf{x}_{\setminus [k]}),$$

where  $n$  is the number of features, and  $\mathbf{x}_{\setminus [k]}$  is the perturbed input whose top- $k$  important features are removed.

- **Comprehensiveness (COMP) (DeYoung et al., 2019)** measures the changes of predictions before and after removing the most important features. A *higher* COMP means a more faithful explanation. Formally,

$$\text{COMP} = \frac{1}{\|K\|} \sum_{k \in K} |f_c(\mathbf{x}) - f_c(\mathbf{x}_{\setminus [k]})|,$$

where  $K$  is  $\{1, \dots, n\}$  for tabular data, and  $\{1\% * n, 5\% * n, 10\% * n, 20\% * n, 50\% * n\}$  for images and graphs. The same setting of  $K$  is adopted for SUFF.

- **Sufficiency (SUFF) (DeYoung et al., 2019)** measures the change of predictions if only the important tokens are preserved. A *lower* SUFF means a more faithful explanation. Formally,

$$\text{SUFF} = \frac{1}{\|K\|} \sum_{k \in K} |f_c(\mathbf{x}) - f_c(\mathbf{x}_{[k]})|,$$

where  $\mathbf{x}_{[k]}$  is the perturbed input with only top- $k$  important features.

## B.4. Compared Methods

**Baselines.** We compare our proposed methods with other state-of-the-art methods. For simplicity, let  $H(\mathbf{x})$  be the Hessian matrix of a neural network  $f$  with respect to  $\mathbf{x}$ . Authors in (Dombrowski et al., 2021; Wang et al., 2020c) deduced that the bound on  $\|H(\mathbf{x})\|_2$  affects explanation robustness regarding  $\ell_p$  norm based manipulations.

- **Vanilla:** It provides the basic ReLU model that is trained without any robust strategies. The other baselines share the same structure with Vanilla model, but use weight decay, distinct activation functions, or extra regularizers. The structure of Vanilla models is in Appendix B.5.2.
- **Weight Decay (WD) (Dombrowski et al., 2021):** Weight decay during training models is supposed to improve the explanation robustness by decreasing the weights of the neural networks.
- **Softplus (SP) (Dombrowski et al., 2019; 2021):** A smaller  $\rho$  in Softplus( $x; \rho$ ) =  $\frac{1}{\rho} \ln(1 + e^{\rho x})$  results in a smoother curvature. Since  $\|H(\mathbf{x})\|_2$  also depends on the maximal values of the activation function’s first and second derivatives, Softplus is used to improve the explanation robustness by virtue of its maximal derivatives being smaller than ReLU’s.

- **Exact-Hessian (Exact-H):** Considering Hessian norm as the regularization during training is a straightforward way to reduce the norm of the Hessian. Specifically,

$$\min_{\mathbf{w}} \mathcal{L}_{total} = \mathcal{L}_{cls}(f(\mathbf{x}, \mathbf{w})) + \lambda \mathbb{E}_{\mathbf{x} \in \mathcal{X}_T} \|H(\mathbf{x})\|_2. \quad (59)$$

Since  $\|H(\mathbf{x})\|_2$  is calculated exactly for each training set sample  $\mathbf{x} \in \mathcal{X}_T$ , this method is denoted as exact-Hessian. Notice that it is usually infeasible to explicitly calculate the Hessian matrix nor its Frobenius norm, thus it is only used on three tabular data.

- **Estimate-Hessian (Est-H) (Dombrowski et al., 2021):** Exact-Hessian is very time-consuming due to the explicit computation of Hessian norm. To apply it to high-dimensional datasets such as images and graphs, the finite difference is used to approximate Hessian norm (Pearlmutter, 1994):  $\|\frac{\nabla f(\mathbf{x} + \kappa \mathbf{v}) - \nabla f(\mathbf{x})}{\kappa}\|_2$ , where  $\kappa \ll 1$  is the

discretization step and  $\mathbf{v}$  can be any vector, and we set  $\mathbf{v} = \frac{\text{sign}(\nabla f(\mathbf{x}))}{\|\text{sign}(\nabla f(\mathbf{x}))\|_2}$  following (Moosavi-Dezfooli et al., 2019).

- **SSR** (Wang et al., 2020c): It sets the largest eigenvalue of the Hessian matrix as the regularization.
- **Adversarial Training (AT)** (Huang et al., 2016; Wong et al., 2020): It trains the model following a min-max approach, e.g.,

$$\min_f \sum_{(\mathbf{x}, y) \in (\mathcal{X}_T, \mathcal{Y}_T)} (\mathcal{L}_{cls}(f; \mathbf{x} + \delta^*, y)), \quad \text{s.t. } \delta^* = \arg \max_{\delta} - \sum_{i=1}^n \sum_{j=k+1}^n u(\mathbf{x} \uparrow \delta, i, j).$$

**Proposed methods.** Based on the defense strategy of maximizing ranking thickness in Sec. 3.2, we propose the following methods to enhance ranking explanations robustness:

- **Robust Ranking Explanation via Thickness (R2ET):** It trains model with Eq. (6) as the objective function to improve the ranking explanation thickness. We try  $h(\mathbf{x}, i, j) = \mathcal{I}_i(\mathbf{x}) - \mathcal{I}_j(\mathbf{x})$  and  $h(\mathbf{x}, i, j) = \exp\{\mathcal{I}_i(\mathbf{x}) - \mathcal{I}_j(\mathbf{x})\}$ , and find that the exponential version benefits from a non-negative range of functions in practice. We report better results from two settings, and similar to the variants of R2ET.
  - **R2ET-mm:** An alternative selection of comparison pairs is proposed in Sec. 3.2.  $k'$  distinct indices of  $i, j$  will be selected, where  $i$  covers the smallest  $k'$  features in the top- $k$ , and  $j$  covers the largest  $k'$  features in the rest. In other words,  $\sum_{i,j} h(\mathbf{x}, i, j)$  for  $k'$  pairs is minimized by such selection. We set  $k' = k$  by default, and the sensitivity of  $k'$  is studied in Appendix B.6.6.
  - **R2ET<sub>\setminus H</sub>:** It serves as the ablation variant of **R2ET** by setting  $\lambda_2 = 0$  in Eq. (6). It strives to broaden the gaps between feature importance directly, and does not care about the curvature. Notice that **Est-H** can be considered another ablation variant of **R2ET** with  $\lambda_1 = 0$ .
- R2ET-mm<sub>\setminus H</sub>:** Similar to **R2ET<sub>\setminus H</sub>**, it is a variant of **R2ET-mm** but does not optimize the Hessian-related term in Eq. (6) ( $\lambda_2 = 0$ ).

## B.5. Target Models

### B.5.1. INTRODUCTION TO SIAMESE NETWORK

An SN predicts the probability that two samples,  $\mathbf{x}^s$  and  $\mathbf{x}^t$ , are from the same class. The SN uses a deep network to embed each input, respectively, and uses a similarity function to measure the similarity of the two inputs. An SN can be considered a binary classifier. Specifically, the prediction for class 1 (two samples from the same class),

```
CNN(
  (cnn): Sequential(
    (view0): Reshape()
    (conv0): Conv2d(1, 8, kernel_size=(3, 3), stride=(1, 1))
    (acti0): ReLU()
    (pool0): MaxPool2d(kernel_size=2, stride=2, padding=0, dilation=1, ceil_mode=False)
    (conv1): Conv2d(8, 16, kernel_size=(3, 3), stride=(1, 1))
    (acti1): ReLU()
    (pool1): MaxPool2d(kernel_size=3, stride=3, padding=0, dilation=1, ceil_mode=False)
    (view1): Reshape()
    (dens0): Linear(in_features=144, out_features=64, bias=True)
    (acti2): ReLU()
    (dens1): Linear(in_features=64, out_features=32, bias=True)
    (acti3): ReLU()
    (dens2): Linear(in_features=32, out_features=10, bias=True)
  )
)
```

Figure 4: Setup of CNN for MNIST

$\Pr(y = 1 | \mathbf{x}^s, \mathbf{x}^t)$ , is

$$f_1^{SN}(\mathbf{x}^s, \mathbf{x}^t; \mathbf{w}) = \text{sim}(\text{emb}(\mathbf{x}^s; \mathbf{w}_0), \text{emb}(\mathbf{x}^t; \mathbf{w}_0); \mathbf{w}_1), \quad (60)$$

and  $f_0^{SN} = 1 - f_1^{SN}$  for class 0.  $\text{sim}(\cdot, \cdot; \mathbf{w}_1)$  is a similarity function, such as the cosine similarity, and  $\text{emb}(\cdot; \mathbf{w}_0)$  is an embedding network, such as GNN.  $\mathbf{w} = \{\mathbf{w}_0, \mathbf{w}_1\}$  is the SN’s parameter set. We denote the ground truth used in SN as  $y^{st} = \mathbb{1}[y^s = y^t]$ , where  $y^s$  is the label of  $\mathbf{x}^s$ . The SN is trained using a classification loss  $\mathcal{L}_{cls}$ , such as the binary cross-entropy loss. To make a prediction for a single input, one can further train a classifier  $f^{CL}$  based on the embedding networks from the SN. For example,  $f^{CL}(\mathbf{x}) = \text{cls}(\text{emb}(\mathbf{x}; \mathbf{w}'_0); \mathbf{w}_2)$ , where  $\mathbf{w}'_0$  can be the same as or retrained based on  $\mathbf{w}_0$  in Eq. (60), and  $\text{cls}(\cdot; \mathbf{w}_2)$  is a classifier such as a linear model with the parameter set  $\mathbf{w}_2$ .

### B.5.2. STRUCTURE OF TARGET MODELS

**Vanilla models for tabular data.** We adopt two-layer neural networks for tabular data. The first layer maps the input space to a 32-dimension hidden space and uses LeakyReLU as the activation function. The second layer maps the hidden space to the output space following a sigmoid function.

**Vanilla models for image data.** We use ResNet18 (He et al., 2016) as the target model on CIFAR-10. For SN on MNIST, we hire a classic CNN as the embedding model, consisting of two convolutional layers with 3\*3 kernels followed by max-pooling and three fully-connected layers; see Fig. 4 for details. We use cosine similarity as the similarity metric. The classifier is a single-layer linear model taking the outputs from the embedding models as inputs.

**Vanilla models for graph data.** For SN on graphs, the embedding model is a two-layer GCN and a mean pooling is used to aggregate node features to graph-level one. The first layer maps the input space to a 256-dimension hidden space and uses ReLU as the activation function. The second layer maps the hidden space to a 128-dimension embedding space.

Then the cosine similarity used to measure the similarity between two embeddings of the pair of input graphs. The classifier is a single-layer linear model taking the outputs from the corresponding embedding models as inputs.

### B.5.3. METHODOLOGY OF TRAINING TARGET MODELS

Except CIFAR-10, we train all the models starting from random initialization by default, although we do provide results based on the retraining schema in B.6.6, where we re-train model based on the high-cAUC Vanilla models. Since it takes a long time to train ResNet on CIFAR-10, target models for CIFAR-10 are retrained from Vanilla model, and retrained models are equipped with softplus as activation function due to the lack of softmax in ResNet. All models are trained on the training set, and the ones with high cAUC for prediction and high P@ $k$  for explanations on the validation set will be adopted as the outstanding models for the corresponding method. Specifically, We choose the last model with cAUC higher than a *threshold* on the validation set. The threshold depends on the Vanilla model’s cAUC. In practice, vanilla models achieve cAUC to 0.87, 0.64, 0.83, 0.99, 0.87, 0.69, and 0.76 on Adult, Bank, COMPAS, MNIST, CIFAR-10, BP, ADHD, respectively. Correspondingly, we set the cAUC threshold for other models as 0.86, 0.63, 0.83, 0.99, 0.86, 0.67, and 0.74. We then select the outstanding models with the highest P@ $k$  out of these high cAUC models on the validation set. If not specified, all results shown in tables and figures are from the test set.

### B.5.4. SALIENCY MAPS OF TARGET MODELS

We use the absolute gradient values as the explanation for tabular datasets. For MNIST, we use the absolute gradient values as the explanations, and normalize it so that the sum of all elements is one. For CIFAR-10, the sum of the absolute gradient values are used as the explanations. For graph data, we use element-wise multiplication of the gradient and the input as the explanation (Adebayo et al., 2018). Since the graphs in BP and ADHD are undirected, we focus on the upper triangular adjacency matrix in the explanation, and then normalize it so that the sum of these elements is one.

## B.6. Experimental Settings and More Results

### B.6.1. GENERAL SETTINGS

**Attack targets on explanation ranking.** The goal of attackers is to find an optimal perturbation  $\delta^*$  on the input  $\mathbf{x}$  to mess up the original feature ranking. Intuitively, the attackers flip the relative ranking between  $(i, j)$  features for as many pairs as possible. Formally, we consider the following

Explanation Ranking Attack (ERAttack) objective:

$$\delta^*(\mathbf{x}) = \arg \min_{\|\delta\|_2 \leq \epsilon} \int_0^1 \sum_{i=1}^k \sum_{j=k+1}^n h(\mathbf{x} + t\delta, i, j) dt. \quad (61)$$

It is infeasible to optimize Eq. (61) by gradient descent directly due to the integration over  $t$ . We propose finding the optimal perturbations in the PGD-style (Madry et al., 2017), which searches the optimal adversarial sample by iteratively moving a small distance toward the goal function. Assume that the ERAttack searches the optimal  $\delta^*(\mathbf{x})$  starting from  $\mathbf{x}^0 := \mathbf{x}$  within  $T$  iterations. We first approximate the integration by summation,  $\frac{1}{T} \sum_{t=1}^T \sum_{i=1}^k \sum_{j=k+1}^n h(\mathbf{x} + \frac{t}{T}\delta, i, j)$ . Instead of directly searching the optimal  $\delta^*$  by solving Eq. (61) for  $\mathbf{x}$ , we decompose the optimization into  $T$  steps. In the  $t$ -th attacking iteration, we search for the optimal perturbation  $\delta^t$  to minimize  $\frac{1}{T} \sum_{i=1}^k \sum_{j=k+1}^n h(\mathbf{x}^t, i, j)$  for the intermediate point  $\mathbf{x}^t := \mathbf{x}^{t-1} + \delta^{t-1}$ . Eventually, the ERAttack ends at an adversarial sample  $\mathbf{x}' = \mathbf{x}^T$  after traveling a distance of  $\epsilon$  for  $T$  iterations. Note that  $\mathbf{x} + \frac{t}{T}\delta$  is not necessarily equivalent to  $\mathbf{x}^t$ , although they are empirically consistent.

**Hyperparameters.** We pick  $k = 8$  for three tabular data,  $k = 100$  for CIFAR-10, and  $k = 50$  for MNIST and graphs by default. We set the maximal training epoch as 300 for three tabular data, 100 for MNIST, and 10 for two graph datasets, BP and ADHD. The maximal retraining epoch for CIFAR-10 is set as 10. Almost all models are guaranteed to converge within given maximal epochs, except when the regularization term weights are too large. The learning rate is set to 1e-2 for three tabular data, 1e-3 for MNIST, 1e-2 for CIFAR-10, and 1e-4 for BP and ADHD. The early stop for three tabular data is 30, and no early stop is set for the image and graph datasets. Except in the sensitivity analysis in Appendix B.6.6, we set  $k' = k$  for R2ET and its variants for three tabular datasets and image datasets, and  $k' = 20$  for BP and ADHD. In each iteration, R2ET maintains the ranking from model in the previous iteration.

As for the hyperparameters used in attacks, we conduct attacks in a PGD-style (Madry et al., 2017) for at most 1000 iterations for tabular datasets, and perturb input with a 1e-3 budget in each iteration. Thus, each input in tabular datasets can be manipulated with at most  $\epsilon = 10^{-3} * 1000 = 1$  budget. The budget is set as  $100 * 5e - 2$  for CIFAR-10, and  $100 * 1e - 2$  for the rest. At each iteration, the infinity norm of the perturbations is restricted to no more than 5 for images and 0.2 for graphs.

**Candidate range of parameters.** We search  $\kappa$  for estimating Hessian norm by the finite differential in Est-H from  $\{1e - 6, 1e - 5, \dots, 1e - 2\}$ .  $\rho$  in SP from  $\{0.5, 1, 5, 10, 100\}$ , and the weight-decay parameter in WD from  $\{5e - 5, 5e - 4, 5e - 3, 1e - 2, 5e - 2\}$ . As for all

other (single) regularization-based methods,  $\lambda$  can be drawn from  $\{0.01, 0.1, 1, 5, 10, 100\}$ . As for the dual regularization methods, such as R2ET, we adopt the following settings for the weights.  $\lambda_1$  and  $\lambda_2$  are selected as the same as the best  $\lambda$  for R2ET $\setminus_H$  and est-H, respectively. Alternatively, we simply set  $\lambda_1 = \lambda_2 = \lambda$ , and  $\lambda$  can be drawn from  $\{0.01, 0.1, 1, 5, 10, 100\}$ .

**Running environment.** We majorly conduct experiments for three tabular data and CIFAR-10 on the following two machines. Both come with a 16-core Intel Xeon processor and four TITAN X GPUs. One installs 16.04.3 Ubuntu with 3.8.8 Python and 1.7.1 PyTorch, and the other installs 18.04.6 Ubuntu with 3.7.6 Python and 1.8.1 PyTorch. The MNIST and graph datasets are run on a machine with two 10-core Intel Xeon processors and five GeForce RTX 2080 Ti GPUs, which installs 18.04.3 Ubuntu with 3.9.5 Python and 1.9.1 PyTorch.

### B.6.2. SETTINGS FOR CORRELATION EXPERIMENTS AND MORE RESULTS

Sec. 5.3 explores the correlation between the manipulation epochs and thickness and Hessian norm, based on R2ET results on COMPAS datasets. Here, we provide more results in terms of different models on various datasets. Specifically, as shown in Fig. 5, we consider different datasets and methods, such as Vanilla, est-H, and R2ET. Since images and graphs have more features than the three tabular datasets, almost all adversarial samples will swap feature pairs under the first epoch of attack. Alternatively, we set the manipulation epoch metric for graph and image datasets to record the first epoch where P@k drops below 0.8. We do not plot the results on Bank dataset, where R2ET achieves 100% P@k. Fig. 5 presents the correlations between manipulation epochs and the other four metrics. Besides thickness measured by adversarial samples and Hessian norm as used in Sec. 5.3, we additionally show the thickness measured by either the average or minimal of a few Gaussian samples. As mentioned in Sec. 3.1, different sampling distribution over  $\mathbf{x}'$  is designed for distinct scenarios. Specifically, when samples  $\mathbf{x}'$  are drawn from Gaussian distribution, the thickness is specific to the ranking robustness under *random noise* (Zhou & Croft, 2006), instead of *adversarial attacks* being evaluated by adversarial samples. Even though the thickness evaluated by Gaussian distribution is not specific to adversarial attacks, it is evident that the corresponding correlations are much higher than that between the manipulation epoch and Hessian norm.

The model-level thickness is defined as the average thickness over all the samples, defined in Eq. (4). We show P@k and model-level thickness in Table 2. Clearly, the models with high P@k performance usually have a relatively large thickness as well, and vice versa.

### B.6.3. MORE RESULTS FOR CASE STUDY

In Sec. 5.4, we demonstrate the robust and plausible advantages of R2ET and R2ET-mm over Vanilla and weight decay methods through case studies. In Fig. 6, we provide the results of other methods mentioned in Sec. 5.1, demonstrating the advantages of R2ET and R2ET-mm over others.

### B.6.4. CONSTRAINED OPTIMIZATION

In Sec. 2, we briefly introduce the general form of constraints for adversarial attacks against explanations. Since defenders can catch adversarial attacks if there are *any* changes in predictions, the attackers must keep *all* predictions, one from the SN, and two from the classifier with respect to the inputs, unchanged during the attacks. We formulate it as a constrained optimization problem. Specifically, we denote the primary objective function Eq. (61) which manipulates the explanations as  $g_0$ , and three constraints used to ensure small predictions changes as  $g_1, g_2, g_3$ , respectively. Here, we use symmetric KL-divergence to measure the changes in predictions before and after perturbations. Naturally, we construct a Lagrangian function connecting the objective function and the constraints with the non-negative Lagrange multiplier  $\gamma = [\gamma_0, \gamma_1, \gamma_2, \gamma_3] \in \mathbb{R}_+^4$ ,

$$\mathcal{L}(\mathbf{x}, \gamma) = \gamma_0 g_0(\mathbf{x}) + \sum_{k=1}^3 \gamma_k g_k(\mathbf{x}). \quad (62)$$

Some previous works manually set  $\gamma$  as a hyperparameter by experience (Dombrowski et al., 2019), which cannot capture the relatives among  $g_k$ . Instead, we care the unsatisfied constraints with higher weights by uplifting  $\gamma_k$  with larger  $g_k$ . Thus, we adopt the following constrained optimization methods to update both primal variables  $\mathbf{x}$  and dual variables  $\gamma$  simultaneously (Rony et al., 2020; Chen et al., 2021):

- **Gradient descent ascent (GDA)** is one of the most popular algorithms to solve the nonconvex-concave minimax problems (Lin et al., 2020). Specifically,

$$\mathbf{x} \leftarrow \mathbf{x} - \eta_x \frac{\partial \mathcal{L}}{\partial \mathbf{x}}, \quad \gamma \leftarrow \gamma + \eta_\gamma \frac{\partial \mathcal{L}}{\partial \gamma}, \quad (63)$$

where  $\eta_x$  and  $\eta_\gamma$  are the learning rates. Notice that  $\frac{\partial \mathcal{L}(\mathbf{x}, \gamma)}{\partial \gamma_k} = g_k, \forall i \in \{1, 2, 3\}$ , and  $\gamma_0$  is passively updated by the normalization  $\sum_{k=0}^3 \gamma_k = 1$  at the end of each iteration.

- **Hedge** is an incarnation of Multiplicative Weights algorithm that updates  $\gamma$  by using exponential factors (Arora et al., 2012). In each iteration, we first normalize  $\gamma$  such that  $\sum_{k=0}^3 \gamma_k = 1$ , and then update  $\gamma$  by

$$\gamma \leftarrow \gamma \odot \exp^{\eta_{Hedge} [g_0, g_1, g_2, g_3]}, \quad (64)$$

where  $\eta_{Hedge} \in \mathbb{R}_+$  is the learning rate,  $\odot$  is the element-wise multiplication, and  $\exp$  is exponential operation.

## Provable Robust Saliency-based Explanations

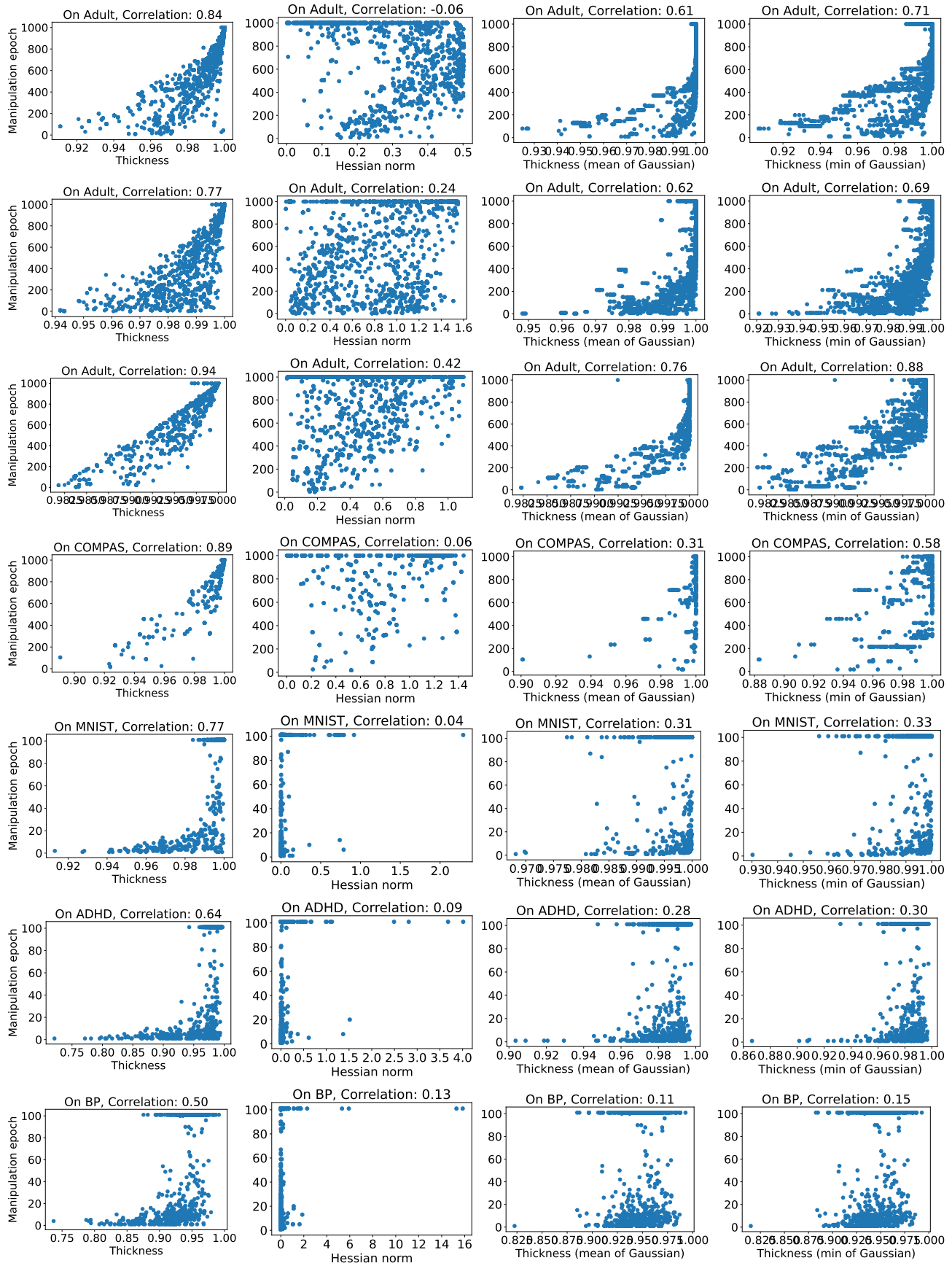


Figure 5: We show the correlation between the manipulation epoch and other metrics, including thickness evaluated by adversarial samples, Hessian norm, and thickness evaluated by (mean and min of) Gaussian samples for different models in various datasets. From top to bottom: Vanilla, est-H models on Adult, respectively. R2ET models on Adult, COMPAS, MNIST, ADHD, and BP, respectively.

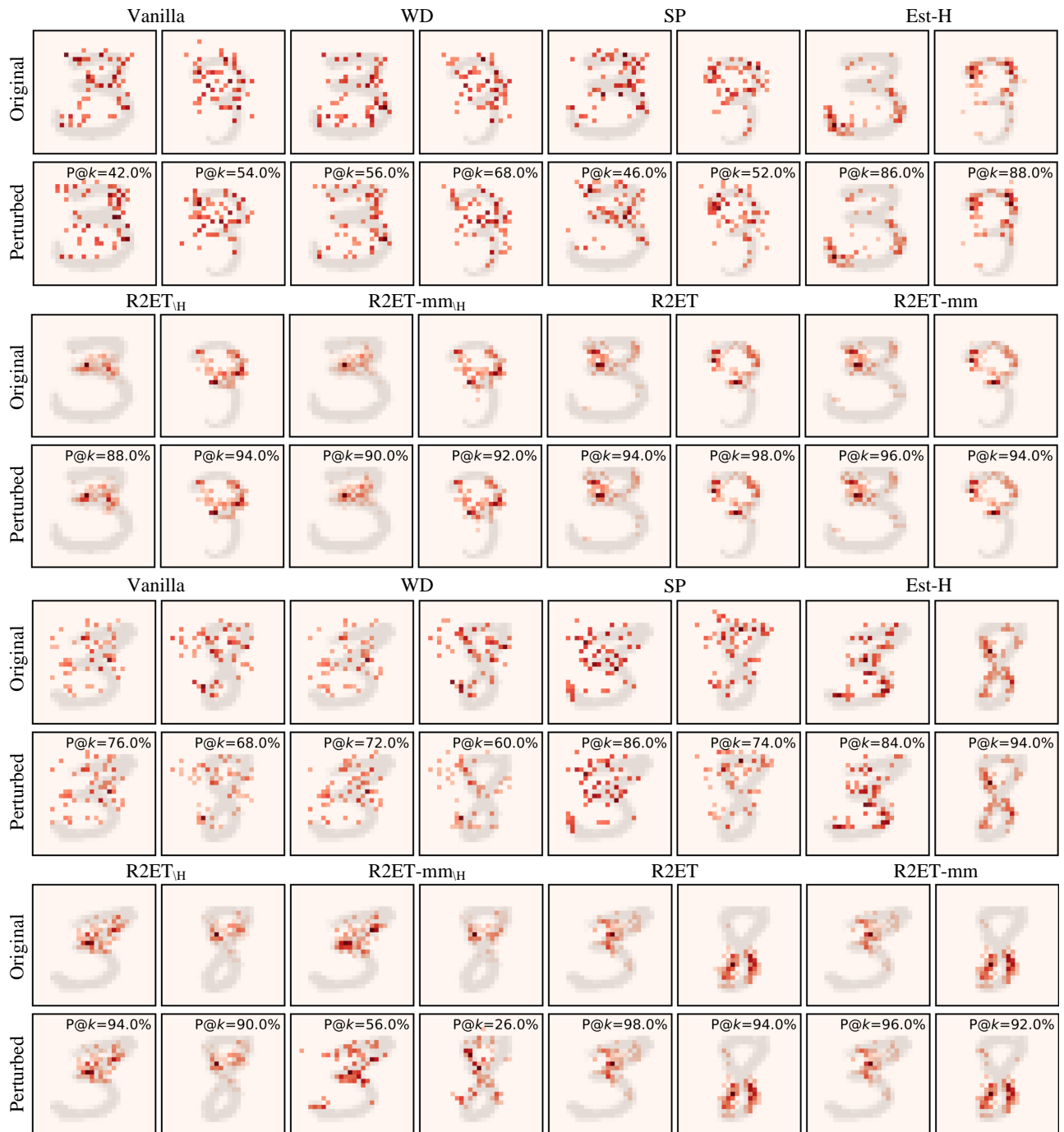


Figure 6: Saliency maps with respect to the original image pair and the image pair perturbed under ERAttack for all methods mentioned in Sec. 5.1 in SNs. The red pixels are the top 50 important features in saliency maps, with darker colors meaning more important.  $P@k$  implies the ratio of the top 50 important features of saliency maps that overlap before and after ERAttack for the corresponding sample.

## Provable Robust Saliency-based Explanations

Table 2:  $P@k$  (shown in percentage) of different robust models (rows) under ERAttack and the values of model-level **thickness**.

Method	Adult	Bank	COMPAS	MNIST	ADHD	BP
Vanilla	87.6 / 0.9889	83.0 / 0.9692	84.2 / 0.9533	59.0 / 0.9725	45.5 / 0.9261	69.4 / 0.9282
WD	91.7 / 0.9960	82.4 / 0.9568	87.7 / 0.9769	59.1 / 0.9732	47.6 / 0.9343	69.4 / 0.9298
SP	<u>97.4 / 0.9983</u>	<u>95.4 / 0.9978</u>	<b>99.5 / 0.9999</b>	62.9 / 0.9771	42.5 / 0.9316	68.7 / 0.9300
Est-H	87.1 / 0.9875	78.4 / 0.9583	82.6 / 0.9557	<u>85.2 / 0.9948</u>	58.2 / 0.9578	<b>75.0 / 0.9356</b>
Exact-H	89.6 / 0.9932	81.9 / 0.9521	77.2 / 0.9382	- / -	- / -	- / -
SSR	91.2 / 0.9934	76.3 / 0.9370	82.1 / 0.9549	- / -	- / -	- / -
AT	68.4 / 0.9372	80.0 / 0.9473	84.2 / 0.9168	56.0 / 0.9639	59.4 / 0.9597	<u>72.0 / 0.9342</u>
R2ET <sub>\H</sub>	<b>97.5 / 0.9989</b>	<b>100.0 / 1.0000</b>	91.0 / 0.9727	82.8 / <b>0.9949</b>	60.7 / 0.9588	70.9 / 0.9271
R2ET-mm <sub>\H</sub>	93.5 / 0.9963	<u>95.8 / 0.9874</u>	<u>95.3 / 0.9906</u>	81.6 / 0.9942	<u>64.2 / 0.9622</u>	<u>72.4 / 0.9342</u>
R2ET	92.1 / 0.9970	80.4 / 0.9344	92.0 / 0.9865	<b>85.7 / 0.9949</b>	<b>71.6 / 0.9731</b>	71.5 / 0.9296
R2ET-mm	87.8 / 0.9943	75.1 / 0.9102	82.1 / 0.9544	<u>85.3 / 0.9948</u>	58.8 / 0.9588	<u>73.8 / 0.9356</u>

- An alternative way to update weights  $\gamma$  is solving a **quadratic programming (QP)** problem

$$\begin{aligned} \max_{\gamma} & \quad \frac{1}{2} \left\| \sum_{k=0}^3 \gamma_k \nabla g_k(\mathbf{x}) \right\|^2, \\ \text{s.t.} & \quad \sum_{k=0}^3 \gamma_k = 1, \quad \gamma_k \geq 0, \forall k \in \{0, \dots, 3\}. \end{aligned} \quad (65)$$

We also consider **unconstrained** attack without any constraints, and **no update** method that fixes the weights to  $\gamma = [0.25, 0.25, 0.25, 0.25]$  in Eq. (62).

In Fig. 7, we show different constrained attack methods in terms of  $P@k$  and sensitivity through scatter plots. For attackers, smaller values of both sensitivity and  $P@k$  are better: smaller sensitivity means that the constraints are satisfied better, and smaller  $P@k$  means that more top- $k$  important features in the explanation are distorted. From methods on the Pareto front, we pick the one with no more than 2 % sensitivity and the smallest  $P@k$ . We mark the attack methods used to evaluate the defense strategies in Table 1 with asterisks in Fig. 7. We do not use constrained attacks on three tabular datasets and MNIST because their sensitivity is 0%. For datasets where constrained attacks are used (BP and ADHD), we compute the metrics in Appendix B.3 by removing the few samples caught by the defenders.

In addition to sensitivity metrics, we also use cAUC and aAUC to measure the performance of constrained attacks in terms of accuracy. As shown in Table 3, the difference between cAUC and aAUC for all methods is no more than 0.01, showing the success of the selected constrained attack to retain the predictions.

### B.6.5. TRADE-OFF BETWEEN ACCURACY AND EXPLANATION ROBUSTNESS

A good defensive strategy should be both robust and accurate. Authors in (Tsipras et al., 2018) find the trade-off between *prediction* robustness and prediction accuracy. This section will explore the trade-off between the *explanation* robustness and prediction performance. Specifically, we study

the relationship between  $P@k$  and cAUC/aAUC for all methods mentioned in Table 1 on MNIST, ADHD, and BP. For a defender, larger values of both  $P@k$  and cAUC/aAUC are better: a higher  $P@k$  means a more robust model, and a higher cAUC/aAUC means a more accurate model. In Fig. 8, the methods on the Pareto front (shown by red lines) cannot be beaten by other methods under both metrics. Apparently, at least one R2ET and its variants are on the Pareto front on all datasets, demonstrating that R2ET and its variants are more advantageous in the trade-off between robustness and accuracy. Furthermore, on MNIST, compared with other methods on the Pareto front, R2ET variants on the Pareto front sacrifice less AUC (less than 2%) but gain significant improvements on  $P@k$  (20% ~ 40%). On BP, Est-H improve  $P@k$  by 0.01 but lost about 4% AUC. R2ET on ADHD with both high AUC and the highest  $P@k$  indicates the possibility that a model can be precise and explanation-robust at the same time.

### B.6.6. SENSITIVITY ANALYSIS

In this section, we consider the impacts of three hyperparameters or settings.

**Impacts of  $k$ .** First, we explore whether different settings of  $k$  result in similar observations and conclusions. As shown in Table 4, similar to the observations when  $k=8$  discussed in Sec.5, R2ET and its variants stay at the top compared with other baselines for various  $k$ . Besides that, SP and est-H are very competitive and sometimes beat R2ET on tabular datasets and MNIST, respectively. However, they cannot perform well on other datasets.

As mentioned in Eq. (5), the gaps of gradients of original inputs positively contribute to the thickness. We present an auxiliary Fig. 9, where the features are sorted in the gradient magnitude descending orderings, and we can easily infer the gaps between any features. Now we focus on the trends of  $k$  taking different values. On the tabular datasets, when  $k = 2$  is small, almost all methods have about 100%  $P@k$ , indicating that even ERAttack cannot effectively ma-

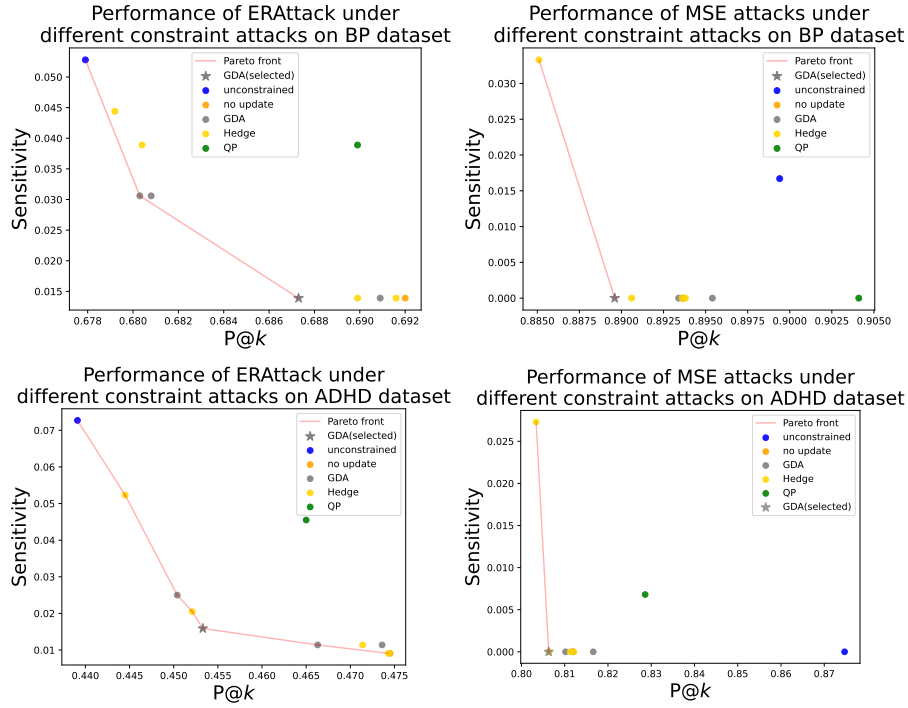


Figure 7: Performance of different constrained ERAttack and MSE attacks on BP and ADHD for Vanilla. Points in different colors represent different constraint attack methods, and the same color represents the same method with a different step-size. The point crossed by the red line is the attack method on the Pareto front, and the asterisk marks the attack method selected to evaluate the defense strategy in Table 1.

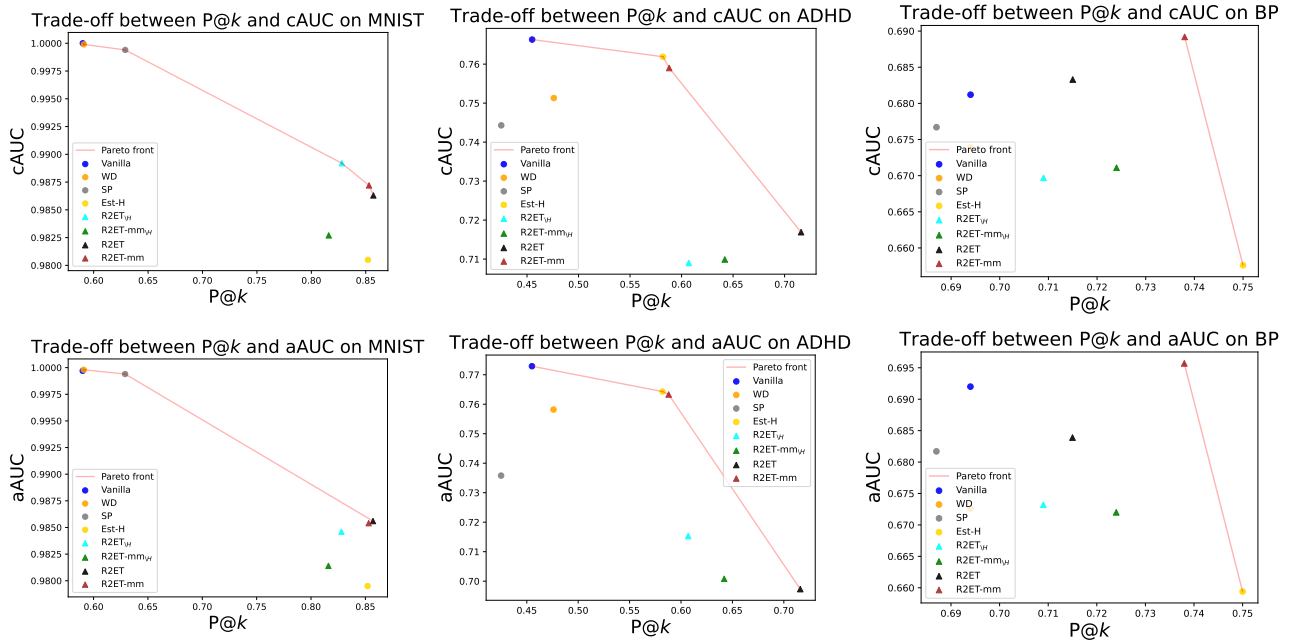


Figure 8: Trade-off between explanation robustness ( $P@k$ ) and prediction performance (cAUC/aAUC) on MNIST, BP and ADHD. The points crossed by the red lines are the methods on the Pareto front, and the triangular markers present R2ET and its variants.

Provable Robust Saliency-based Explanations

Table 3: cAUC/aAUC of SNs trained by different methods under ERAttack and MSE attack on ADHD and BP.

Method	ADHD(ERAttack)	BP(ERAttack)	ADHD(MSE attack)	BP(MSE attack)
Vanilla	0.7663 / 0.7729	0.6812 / 0.6920	0.7663 / 0.7659	0.6744 / 0.6776
WD	0.7513 / 0.7582	0.6739 / 0.6726	0.7508 / 0.7542	0.6753 / 0.6722
SP	0.7443 / 0.7358	0.6767 / 0.6817	0.7395 / 0.7375	0.6706 / 0.6763
Est-H	0.7619 / 0.7643	0.6576 / 0.6594	0.7618 / 0.7633	0.6572 / 0.6558
AT	0.7325 / 0.7277	0.6405 / 0.6347	0.7649 / 0.7659	0.6728 / 0.6773
R2ET <sub>\H</sub>	0.7090 / 0.7153	0.6697 / 0.6732	0.7061 / 0.7058	0.6665 / 0.6700
R2ET-mm <sub>\H</sub>	0.7099 / 0.7008	0.6711 / 0.6720	0.7020 / 0.7014	0.6642 / 0.6654
R2ET	0.7169 / 0.6973	0.6833 / 0.6839	0.7049 / 0.7104	0.6738 / 0.6780
R2ET-mm	0.7590 / 0.7633	0.6892 / 0.6957	0.7583 / 0.7580	0.6841 / 0.6852

Table 4: P@k (shown in percentage) of models trained by different methods under ERAttack. Three numbers for each method on tabular datasets present the results when k is 2, 5, and 8, respectively. And k is set to 10, 30, and 50 on the rest datasets, respectively. Exact-H and SSR are only applicable on tabular datasets due to high time complexity.

Method	Adult	Bank	COMPAS
Vanilla	79.3 / 81.9 / 87.6	97.9 / 81.4 / 83.0	66.1 / 78.1 / 84.2
WD	100.0 / 99.8 / 91.7	97.2 / 92.5 / 82.4	100.0 / 88.1 / 87.7
SP	100.0 / 100.0 / 97.4	100.0 / 99.4 / 95.4	100.0 / 100.0 / 99.5
Est-H	100.0 / 92.9 / 87.1	86.9 / 83.9 / 78.4	99.9 / 83.9 / 82.6
Exact-H	100.0 / 92.3 / 89.6	92.9 / 89.1 / 81.9	79.9 / 79.3 / 77.2
SSR	100.0 / 92.9 / 91.2	87.0 / 85.8 / 76.3	87.4 / 87.1 / 82.1
R2ET <sub>\H</sub>	100.0 / 98.5 / 97.5	100.0 / 96.0 / 100.0	84.0 / 98.1 / 91.9
R2ET-mm <sub>\H</sub>	100.0 / 99.8 / 93.5	99.2 / 94.8 / 95.8	100.0 / 83.7 / 95.3
R2ET	100.0 / 93.2 / 92.1	100.0 / 91.8 / 80.4	79.4 / 88.8 / 92.0
R2ET-mm	100.0 / 99.7 / 87.8	98.6 / 92.2 / 75.1	89.0 / 89.0 / 82.1

Method	MNIST	ADHD	BP
Vanilla	51.6 / 56.7 / 59.4	39.4 / 43.2 / 45.3	63.8 / 67.3 / 68.7
WD	51.6 / 56.6 / 59.9	41.0 / 46.3 / 48.6	63.6 / 68.0 / 68.8
SP	54.9 / 60.5 / 63.1	39.4 / 42.7 / 44.7	63.9 / 66.9 / 67.9
Est-H	80.2 / 82.9 / 84.5	53.3 / 56.4 / 57.1	70.8 / 74.8 / 74.3
R2ET <sub>\H</sub>	77.6 / 80.7 / 82.3	59.3 / 62.6 / 63.1	64.5 / 69.3 / 71.4
R2ET-mm <sub>\H</sub>	76.5 / 80.0 / 81.9	57.2 / 62.3 / 64.3	67.6 / 71.5 / 73.1
R2ET	81.4 / 84.1 / 85.3	70.7 / 74.1 / 73.8	66.1 / 70.5 / 72.2
R2ET-mm	80.6 / 83.5 / 84.9	55.3 / 58.5 / 60.1	69.4 / 74.2 / 75.1

nipulate the ranking in such scenarios. This observation occurs in most models because the top 2 features are much more significant than the rest. In Fig. 9, the most important feature’s magnitude is significantly larger than the rest on Bank, and thus Vanilla has a high P@k (97.9). However, there is a narrow margin between the top 2 and top 3 features on COMPAS, and attackers can easily flip their relative rankings, thus Vanilla’s P@k reduces to around 2/3. When k = 5 is larger, P@k of most non-ranking-specific methods reduce to 90% in Adult and Bank and 80% in COMPAS. P@k further significantly reduces when k=8. The key reason for the reduction is that the gaps among features on the

“long tails” are significantly smaller than those on the top, and usually minor perturbation is needed for a successful flip. On MNIST, BP and ADHD, P@k for most methods increases as k grows. It seems that all methods are more efficient against ERAttack with larger k. However, the *absolute number* of success manipulations for top-k features increases for larger k. Take Vanilla on MNIST as an example, ERAttack distorts the model’s 5 features when k=10, and about 40% \* 50=20 features when k=50. Since ERAttack uses the same budget for different k, it becomes harder for ERAttack to manipulate more features simultaneously (for larger k). However, it indeed kicks off more features

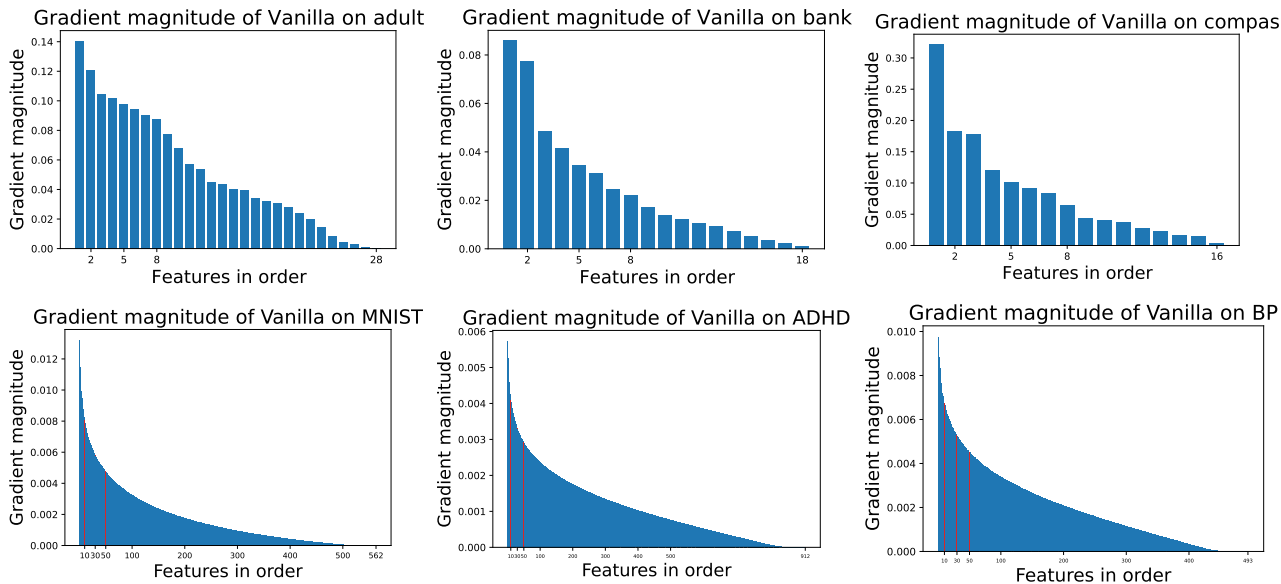


Figure 9: We order the features based on the *Vanilla* model’s gradient magnitude with respect to each original inputs on different datasets. Notice that these figures would differ for various models.

from the top positions due to narrower margins on the long tail.

**Impacts of the number of selected pairs.** As discussed in Sec. 3.2, we can pick only  $k' \leq k$  number of pairs in both R2ET and R2ET-mm methods. For R2ET, a smaller  $k' \leq k$  means that  $\sum_{i=k-k'+1}^{k-1} h(\mathbf{x}, i, k) + \sum_{j=k+1}^{k+k'+1} h(\mathbf{x}, k, j)$ . Here we explore the impacts of  $k'$  in terms of the performance of R2ET and its variants. Notice that R2ET $\setminus_H$  and R2ET-mm $\setminus_H$  are the two best variants in tabular datasets. Thus we conduct a sensitivity analysis of these two methods on Bank dataset. We set  $k = 8$ , and change  $k'$  from 1 to  $k$ .

As shown in Fig. 10, R2ET $\setminus_H$  and R2ET-mm $\setminus_H$  perform much better when  $k' > 4$  than those with  $k' \leq 4$ . Apparently, when more pairs of features are taken into consideration, R2ET and its variants have a more comprehensive view of feature rankings to maintain the rankings better. It is also worth noting that R2ET $\setminus_H$  and R2ET-mm $\setminus_H$  outperform almost all baselines, except for SP, for all  $k'$ .

**Impacts of pretrain / retrain.** Lastly, we explore how good are these methods when applying them in the retrain schema. In previous experiments, all methods are trained starting from random states. We now retrain the Vanilla models with these methods for ten epochs at most. Since the Vanilla model has already converged and reached a good cAUC, we assume that the Vanilla model’s explanation ranking is an excellent reference, and thus these robust methods try to maintain the Vanilla model’s rankings. Thus, we will terminate the retraining phase if  $P@k$  between Vanilla model’s explanation ranking and the retrain model’s ranking significantly drops, or the retrain model’s cAUC drops a lot.

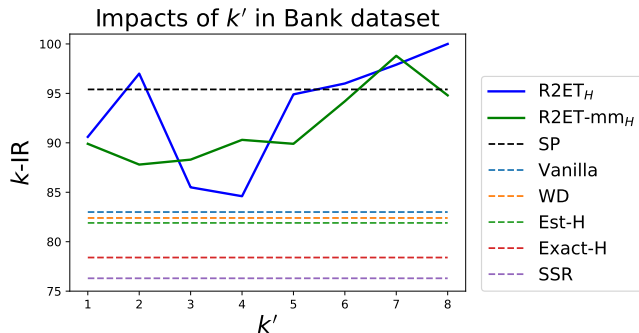


Figure 10: Sensitivity analysis on the number of selected pairs. R2ET $\setminus_H$  and R2ET-mm $\setminus_H$  are examined in Bank dataset.

Table 5 present the results for comparing two training schemas. Since the baseline SP changes the models’ structure (activation function), we do not consider it here. Instead, we add one more baseline, CL (Hein & Andriushchenko, 2017), because retraining demands much fewer training epochs, thus its time complexity is acceptable. More details for CL can be found in Sec. 3.2. Besides that, *none* of retrain models by Exact-H and SSR can maintain Vanilla model’s explanation rankings and cAUC at the same time in Bank dataset, and thus both are not applicable.

## B.7. SG and IG as explanation methods

Instead of Simple Gradient of the models with respect to inputs as the explanations, we adopt two other gradient-based explanation methods, SmoothGrad (SG) (Smilkov

Table 5: P@k (shown in percentage) of models trained by different methods under ERAttack ( $k = 8$ ). Two numbers indicate the performance of models being trained from a **random state** or **retrained** from the Vanilla models.

Method	Adult	Bank	COMPAS
Vanilla	87.6 / 87.6	83.0 / 83.0	84.2 / 84.2
WD	91.7 / 88.3	82.4 / 82.1	87.7 / 82.7
CL	- / 93.1	- / 100.0	- / 87.1
Est-H	87.1 / 92.1	78.4 / 85.2	82.6 / 85.1
Exact-H	89.6 / 88.7	81.9 / -	77.2 / 87.0
SSR	91.2 / 88.7	76.3 / -	82.1 / 86.1
R2ET <sub>\H</sub>	97.5 / 100.0	100.0 / 100.0	91.9 / 97.8
R2ET-mm <sub>\H</sub>	93.5 / 100.0	95.8 / 98.3	95.3 / 95.6
R2ET	92.1 / 92.6	80.4 / 86.2	92.0 / 85.1
R2ET-mm	87.8 / 91.6	75.1 / 86.2	82.1 / 87.4

et al., 2017) and Integrated Gradients (IG) (Sundararajan et al., 2017).

SG takes random samples in a small neighborhood of input  $\mathbf{x}$ , and calculates the average of the saliency maps for these neighboring samples as the final saliency map for  $\mathbf{x}$ . Particularly, we consider adding a Gaussian noise obeying  $\mathcal{N}(0, \sigma^2 I)$  to the original inputs,

$$\mathcal{I}_{SG}(\mathbf{x}) = \frac{1}{M} \sum \mathcal{I}(\mathbf{x} + \delta), \quad \text{s.t. } \delta \sim \mathcal{N}(0, \sigma^2 I).$$

$M$  is the number of neighboring samples. In practice, we set  $M=50$  for all datasets, and  $\sigma^2 = 0.5, 25.5^2$  and  $0.01$  for tabular, image and graph datasets, respectively.

IG is defined as the integration of the saliency maps along a path from a reference point  $\mathbf{x}^0$  to input  $\mathbf{x}$ . Formally,

$$\mathcal{I}_{IG}(\mathbf{x}) = (\mathbf{x} - \mathbf{x}^0) \int_{\alpha=0}^1 \frac{\partial f(\mathbf{x}^0 + \alpha(\mathbf{x} - \mathbf{x}^0))}{\partial \mathbf{x}} d\alpha.$$

In practice, we set the reference point  $\mathbf{x}^0$  as the all-zero vector, and approximate the integration by interpolating 100 samples between  $\mathbf{x}^0$  and  $\mathbf{x}$ .

**Experimental results.** Table 6 report P@k values under ERAttack when adopting Simple Gradient, SG and IG as explanation methods, respectively. Overall, SG and IG generate more robust explanations for most of the models under attacks. Furthermore, the relative performance rankings among different training methods remain the same, no matter Simple Gradient, SG or IG is adopted as the explanation methods. Especially, R2ET and its variants achieve the best performance in most datasets and are compatible with other gradient-based explanation methods, such as SG and IG, for even better robustness.

Since R2ET and other baselines are *training* methods, we do NOT encourage comparing R2ET with SG, since SG is an *explanation* method. Both training method and explanation

method change if comparing (Vanilla + SG) with (R2ET + Simple Gradient). Instead, we compare (Vanilla + Simple Gradient) with (R2ET + Simple Gradient) to investigate the superiority of training methods, or to compare (R2ET + IG) with (R2ET + SG) to explore the stability of the explanation methods.

### B.8. Faithfulness of explanations on different models

We report the faithfulness of explanations evaluated by three widely used metrics, DFFOT, COMP and SUFF, in Table 7.

Provable Robust Saliency-based Explanations

Table 6: P@k (shown in percentage) of different models under ERAttack, k = 8 for the first three dataset and k = 50 for the rest. We report P@k for **Simple Gradient** (from Table 1)/SG/IG for each method-dataset combination.

Method	Adult	Bank	COMPAS
Vanilla	87.6 / 94.0 / <b>71.8</b>	83.0 / 90.0 / 88.1	84.2 / 92.9 / 94.7
WD	91.7 / 97.3 / 55.5	82.4 / 91.3 / 85.7	87.7 / 97.4 / 99.1
SP	<u>97.4 / 95.3 / 63.9</u>	95.4 / 96.7 / <u>99.9</u>	<b>99.5 / 100.0 / 100.0</b>
Est-H	87.1 / 93.1 / 61.5	78.4 / 87.3 / 82.4	82.6 / 89.9 / 89.9
Exact-H	89.6 / 95.8 / 62.1	81.9 / 89.7 / 90.0	77.2 / 91.6 / 90.8
SSR	91.2 / 93.0 / 62.5	76.3 / 84.9 / 85.4	82.1 / 96.2 / <u>99.5</u>
AT	68.4 / 76.6 / 60.0	80.0 / 85.9 / 82.6	84.2 / 85.9 / 82.4
R2ET <sub>\H</sub>	<b>97.5 / 97.5 / 57.3</b>	<b>100.0 / 100.0 / 100.0</b>	91.0 / 96.6 / 93.6
R2ET-mm <sub>\H</sub>	93.5 / 97.4 / 55.9	<u>95.8 / 97.0 / 96.3</u>	<u>95.3 / 99.1 / 95.5</u>
R2ET	92.1 / <b>99.3</b> / 54.0	80.4 / 88.9 / 84.4	92.0 / <u>99.7</u> / <b>100.0</b>
R2ET-mm	87.8 / <u>98.6</u> / 54.2	75.1 / 85.1 / 80.3	82.1 / 93.5 / <u>99.5</u>

Method	MNIST	ADHD	BP
Vanilla	59.0 / 67.9 / 82.8	45.5 / 39.0 / 56.9	69.4 / 59.6 / 60.8
WD	59.1 / 68.3 / 83.0	47.6 / 42.3 / 57.2	69.4 / 61.8 / 63.9
SP	62.9 / 69.0 / 85.4	42.5 / 36.9 / 54.9	68.7 / 58.6 / 60.5
Est-H	85.2 / 87.9 / 89.5	58.2 / 48.9 / 54.7	<b>75.0</b> / 63.0 / 58.5
Exact-H	- / - / -	- / - / -	- / - / -
SSR	- / - / -	- / - / -	- / - / -
AT	56.0 / 61.5 / 79.3	59.4 / 41.2 / 43.0	72.0 / 56.7 / 54.4
R2ET <sub>\H</sub>	82.8 / 87.1 / 89.0	60.7 / 56.9 / <u>61.9</u>	70.9 / 64.2 / <b>66.0</b>
R2ET-mm <sub>\H</sub>	81.6 / 86.8 / 88.7	<u>64.2 / 59.5 / 61.9</u>	72.4 / <u>65.5</u> / 64.1
R2ET	<b>85.7 / 88.5 / 90.4</b>	<b>71.6 / 67.2 / 65.8</b>	71.5 / 64.0 / <u>65.0</u>
R2ET-mm	<u>85.3 / 88.3 / 90.1</u>	58.8 / 50.1 / 51.4	<u>73.8 / 65.6</u> / 63.9

Table 7: Faithfulness of explanations evaluated by DFFOT (↓) / COMP (↑) / SUFF (↓).

Method	Adult	Bank	COMPAS	MNIST	ADHD	BP
Vanilla	0.24 / 0.43 / 0.18	0.23 / 0.14 / 0.04	<b>0.17</b> / 0.37 / 0.14	0.37 / 0.16 / 0.23	0.51 / 0.05 / 0.28	0.40 / 0.06 / 0.29
WD	0.45 / 0.47 / 0.23	0.36 / 0.27 / 0.07	0.29 / 0.41 / 0.18	0.37 / 0.16 / 0.22	0.49 / 0.06 / 0.27	<b>0.35</b> / 0.05 / 0.33
SP	0.43 / 0.47 / 0.25	0.35 / 0.31 / 0.07	0.29 / <b>0.45</b> / 0.18	0.38 / 0.15 / 0.22	<b>0.30</b> / 0.10 / 0.34	<u>0.38</u> / 0.06 / 0.30
Est-H	0.44 / 0.44 / 0.24	0.18 / 0.21 / 0.06	0.27 / 0.42 / 0.17	0.23 / <u>0.24</u> / <b>0.18</b>	0.59 / 0.04 / <u>0.26</u>	0.45 / 0.05 / <b>0.24</b>
Exact-H	0.43 / 0.46 / 0.23	0.19 / 0.14 / 0.04	0.30 / 0.40 / 0.18	- / - / -	- / - / -	- / - / -
SSR	0.54 / 0.39 / 0.21	0.46 / 0.04 / <b>0.01</b>	0.32 / 0.43 / 0.18	- / - / -	- / - / -	- / - / -
AT	<u>0.16</u> / 0.14 / <b>0.08</b>	0.19 / 0.10 / <u>0.03</u>	<u>0.24</u> / 0.10 / <b>0.07</b>	0.40 / 0.12 / 0.28	<u>0.35</u> / 0.10 / <u>0.26</u>	0.46 / <u>0.06</u> / <u>0.25</u>
R2ET <sub>\H</sub>	<b>0.13</b> / <b>0.50</b> / 0.14	0.34 / <u>0.32</u> / 0.10	<b>0.17</b> / 0.40 / 0.17	0.23 / 0.22 / <u>0.19</u>	0.38 / <u>0.13</u> / 0.37	0.43 / <b>0.07</b> / 0.29
R2ET-mm <sub>\H</sub>	0.42 / 0.47 / 0.22	0.34 / <b>0.41</b> / 0.14	0.25 / 0.42 / 0.17	0.25 / 0.22 / 0.21	0.37 / <b>0.17</b> / 0.37	0.42 / <b>0.07</b> / 0.29
R2ET	0.32 / 0.46 / 0.19	<b>0.11</b> / 0.24 / 0.07	0.27 / 0.39 / 0.17	<b>0.18</b> / <b>0.26</b> / 0.23	0.48 / 0.12 / <u>0.26</u>	0.42 / <b>0.07</b> / 0.29
R2ET-mm	0.38 / <u>0.48</u> / 0.20	<u>0.12</u> / 0.21 / 0.08	0.28 / <u>0.44</u> / 0.15	<u>0.19</u> / <b>0.26</b> / 0.22	0.50 / 0.04 / <b>0.25</b>	0.45 / 0.05 / 0.29